nature plants

Article

https://doi.org/10.1038/s41477-025-01940-y

Structural basis for the activation of plant bunyavirus replication machinery and its dual-targeted inhibition by ribavirin

Received: 6 March 2024

Accepted: 6 February 2025

Jia Li[1,2,3,7], Lei Cao[4,7], Yaqian Zhao[1,2,3], Jinghan Shen[1,2,3], Lei Wang[4], Mingfeng Feng[1,2,3], Min Zhu[1,2,3], Yonghao Ye[1,2,3], Richard Kormelink[5], Xiaorong Tao[1,2,3] ✉ & Xiangxi Wang[4,6] ✉

Despite the discovery of plant viruses as a new class of pathogens over a century ago, the structure of plant virus replication machinery and antiviral pesticide remains lacking. Here we report five cryogenic electron microscopy structures of a ~330-kDa RNA-dependent RNA polymerase (RdRp) from a devastating plant bunyavirus, tomato spotted wilt orthotospovirus (TSWV), including the apo, viral-RNA-bound, base analogue ribavirin-bound and ribavirin-triphosphate-bound states. They reveal that a flexible loop of RdRp's motif F functions as 'sensor' to perceive viral RNA and further acts as an 'adaptor' to promote the formation of a complete catalytic centre. A ten-base RNA 'hook' structure is sufficient to trigger major conformational changes and activate RdRp. Chemical screening showed that ribavirin is effective against TSWV, and structural data revealed that ribavirin disrupts both hook-binding and catalytic core formation, locking polymerase in its inactive state. This work provides structural insights into the mechanisms of plant bunyavirus RdRp activation and its dual-targeted site inhibition, facilitating the development of pesticides against plant viruses.

The discovery of tobacco mosaic virus in the late nineteenth century led to the recognition of viruses as a new class of pathogen and the foundation of virology as a discipline. Subsequent studies on plant viruses have contributed greatly to the development of modern virology and molecular biology fields. For instance, the demonstration of viral RNA (vRNA) itself being infectious, and the discovery as well as elucidation of RNA interference as an antiviral defence strategy, were seminal in popularizing these disciplines[1,2]. Plant viruses are known to cause severe quality and yield losses in agricultural crops with an estimated economic impact of over US$30 billion annually, posing a major threat to global food security[3,4]. At present, planting disease-resistant cultivars and applying insecticides to manage insect vectors are the primary methods employed to prevent viral infections and reduce disease losses. However, for plants that have already been infected by viruses, there are currently no effective antiviral drugs for treatment.

In the past decade, numerous efforts have been made towards understanding polymerase structures and the replication mechanism

---

[1]State Key Laboratory of Agricultural and Forestry Biosecurity, Nanjing Agricultural University, Nanjing, China. [2]Key Laboratory of Integrated Management of Crop Disease and Pests, Ministry of Education, Nanjing Agricultural University, Nanjing, China. [3]State and Local Joint Engineering Research Center of Green Pesticide Invention and Application, Nanjing Agricultural University, Nanjing, China. [4]CAS Key Laboratory of Infection and Immunity, National Laboratory of Macromolecules, Institute of Biophysics, Chinese Academy of Sciences, Beijing, China. [5]Laboratory of Virology, Department of Plant Sciences, Wageningen University, Wageningen, the Netherlands. [6]University of Chinese Academy of Sciences, Beijing, China. [7]These authors contributed equally: Jia Li, Lei Cao. ✉e-mail: taoxiaorong@njau.edu.cn; xiangxi@ibp.ac.cn

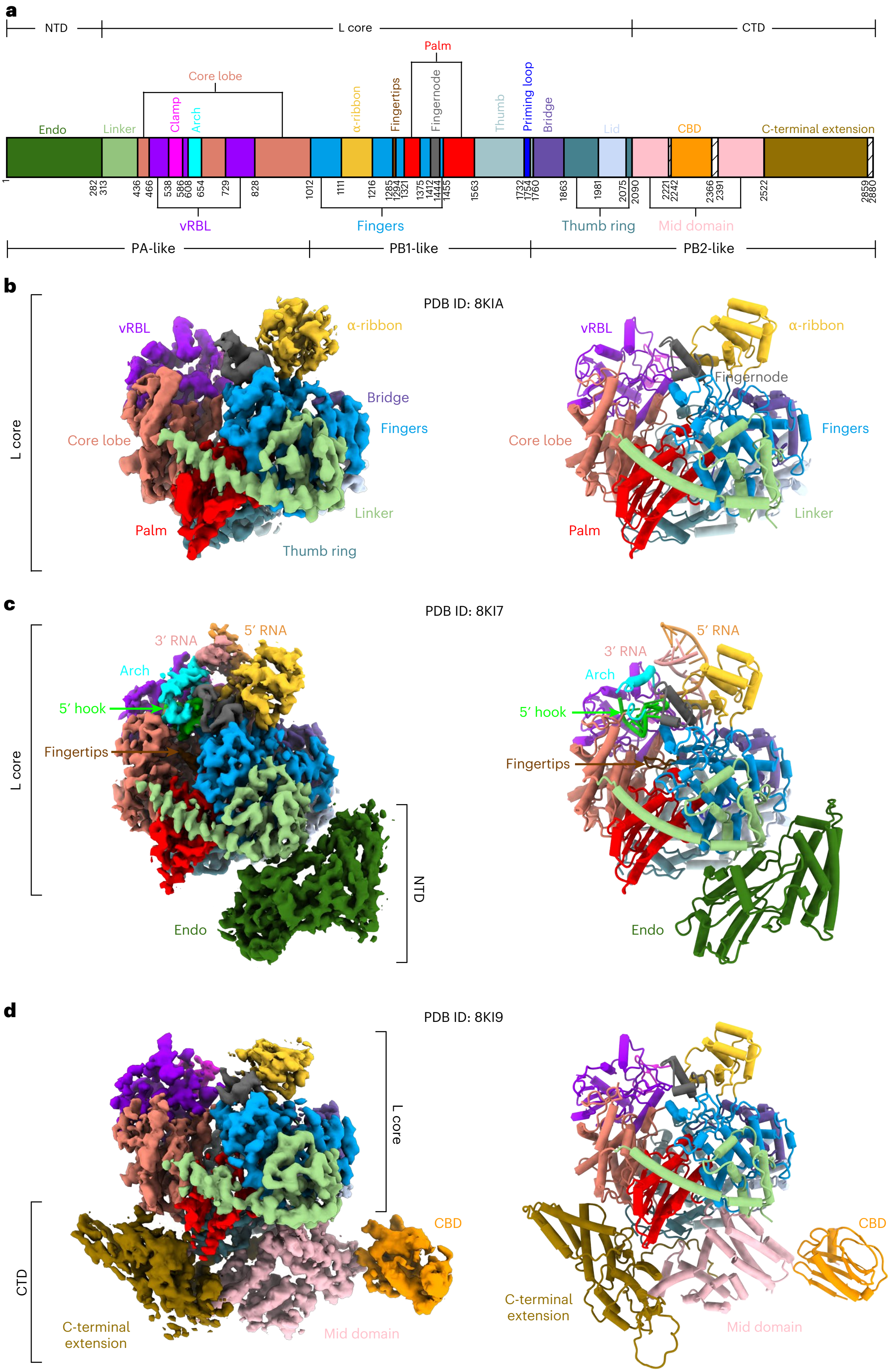

Fig. 1 | Overall structure of TSWV L protein. **a**, Domain architecture of the TSWV L protein. NTD, N-terminal domain; vRBL, vRNA binding lobe; CBD, cap-binding domain; Mid domain, middle domain. **b**–**d**, Cryo-EM maps and cartoon representations of the apo L-core (PDB ID: 8KIA) (**b**), vRNA-promoter-bound L (PDB ID: 8KI7) (**c**) and apo L containing the CTD (PDB ID: 8KI9) (**d**). The structures are coloured by domain with the same colour code as in **a**. 3′ RNA and 5′ RNA are shown in soft red and bright orange, respectively. The 5′ hook is highlighted in lime green.

of human and animal viruses, to help in the design and development of compounds targeting this machinery with high efficacy and exhibiting broad-spectrum antiviral activity[5–7]. The RNA-dependent RNA polymerases (RdRps) from the orders *Articulavirales* and *Bunyavirales* have received particular interest because some of their members (that is, influenza virus, Crimean–Congo haemorrhagic fever virus, Rift Valley fever virus (RVFV) and Lassa virus (LASV)) have high epidemic potential and we lack antivirals or vaccines for them. In recent years, these studies have provided structures for the RdRp of influenza virus[8–13], La Crosse virus (LACV)[14–16], RVFV[17], severe fever with thrombocytopenia syndrome virus (SFTSV)[18–20], Hantaan virus (HTNV)[21,22], Sin Nombre virus (SNV)[23], LASV and Machupo virus (MACV); for the latter two, studies have also provided their structures in the presence of their cognate regulatory Z proteins[24–27].

The International Committee on Taxonomy of Viruses lists more than 2,100 different species of plant viruses so far[4]; to our knowledge, no structure has been resolved for any plant virus replication machinery. Gaps in our understanding of the structure of plant virus replication machinery, which plays a crucial role in the life cycles of viruses, are hampering the development of pesticides against plant viruses. More than 80% of plant viruses are RNA viruses and replicate in the cytoplasm via a viral-encoded RdRp[4]. Tomato spotted wilt orthotospovirus (TSWV) is a global negative-sense plant RNA virus with a segmented genome in the family Tospoviridae of the order Bunyavirales, and its encoded RdRp (also known as the L protein; ~330 kDa) is one of the largest RdRps of all plant viruses[28–31]. The TSWV L protein is also larger than most animal-infecting viral polymerases of known structure (typically ranging from ~50 to 250 kDa)[5,32–35]. In this study we present cryogenic electron microscopy (cryo-EM) structures of full-length TSWV RNA polymerase and provide insights into its activation mechanism and its dual-targeted inhibition by ribavirin.

Results

Overall structure

We determined the cryo-EM structure of both the apo L (L protein without RNA) and the RNA-bound L (L protein in complex with the viral genomic RNA) following successful expression and purification of the full-length L protein of TSWV in High Five insect cells. In the apo-L grids, the major class of particles represented the apo-core structure, which consisted of the polymerase core exclusively and was resolved at a resolution of 3.9 Å (Fig. 1a,b and Supplementary Fig. 1). Density for the amino-terminal domain and the carboxy-terminal domain (CTD) was missing in the electron maps, probably due to the intrinsic flexibility associated with these domains. However, the addition of the vRNA promoter (5′ vRNA$_{(1–17\ \text{nucleotides (nts)})}$ and 3′ vRNA$_{(1–17\ \text{nts})}$) resulted in an ordered endonuclease (endo) region in the major class identified through 3D classification. Furthermore, the resolution of this structure was improved to 3.7 Å (Fig. 1a,c and Supplementary Fig. 2). The polymerase cores of the L–5′3′-vRNA complex with endo and the L–5′3′-vRNA complex without endo showed no significant differences (Supplementary Fig. 3). When viral 5′ vRNA$_{(1–10\ \text{nts})}$ was added, an additional density corresponding to the CTD was observed in only 4% of the particles. After refinement and post-processing, the overall resolution of TSWV L containing the CTD was up to 4.0 Å (Fig. 1a,d and Supplementary Fig. 4).

The structure of TSWV L can be divided into three distinct regions, analogous to the influenza virus polymerase subunits: the N-terminal PA-like region (residues 1–1012), the central PB1-like region (RdRp, residues 1013–1760) and the C-terminal PB2-like region (residues 1761–2880) (Fig. 1a). Despite significant differences in primary sequence and molecular weight, the overall architecture of TSWV L exhibits remarkable similarity to other structurally characterized polymerases of segmented negative strand RNA viruses (sNSVs) (Extended Data Fig. 1). According to the alignment with the influenza polymerase subunits, the TSWV RNA polymerase core, which forms a globular structure, covers the central PB1-like region and the C-terminal part of the PA-like region as well as the N-terminal part of the PB2-like region (Fig. 1a,b). The PB1-like region of TSWV L adopts the characteristic right-hand fold with canonical fingers, thumb and palm subdomains commonly observed in polymerase domains (Extended Data Fig. 1). The endo domain of TSWV L is larger than those of other structurally characterized polymerases (~310 residues versus ~200 residues), primarily due to the presence of additional helices at the N-terminal region of the endo domain. However, all these domains, belonging to the PD-(D/E)-K superfamily of nucleases, share a common two-lobed, kidney-shaped architecture (Extended Data Fig. 2a–e). DALI[36] blast showed that the N-lobe composed of five helices (alpha 1–4 and 10) shares highly similar structural features with an iron-binding protein (PDB ID: 6N63) (Extended Data Fig. 2f). The CTD domain of TSWV L is notably more distinct in size and folding, comprising approximately 800 residues, in contrast to the 400–500 residues found in other sNSVs. It consists of three distinct domains: a cap-binding domain, a middle domain and a C-terminal extension (Extended Data Figs. 3 and 4). The endo domain and CTD extend outward from the core and face each other across a solvent channel in the superposed structure (Fig. 1c,d and Supplementary Fig. 5).

Conformational changes upon vRNA promoter binding

The highly conserved and complementary 5′ and 3′ termini of sNSVs genomic elements play crucial roles as promoters for both transcription and replication. Here we observed that the 5′ and 3′ ends form a continuous double-stranded region encompassing both a proximal and a distal duplex in the TSWV L structure (Figs. 1c and 2a), in contrast to the presence of only a distal duplex in both influenza virus and the other bunyavirus polymerases (Extended Data Fig. 5). The proximal duplex is formed through complementary base pairing of nucleotides 4–10 of the 5′ end with nucleotides 4–10 of the 3′ end. The distal duplex is formed by complementary base pairing of nucleotides 11–13 of the 5′

Fig. 2 | vRNA promoter binding and structural changes. a, Structure and schematic representation of the vRNA promoter, with base pairings indicated by lines. The proximal and distal duplexes are outlined, while RNA nucleotides that are present but not visible are depicted in grey. **b**, Global rearrangements of L structure upon vRNA promoter binding. The structures of apo L (light grey; PDB ID: 8KIA) and vRNA-bound L (coloured; PDB ID: 8KI7) are superimposed. Movement and ordered domains are indicated. **c**, View of the right-hand-like RdRp showing the ordered active site in vRNA-bound L (coloured), which is disordered in the apo form (light grey). The active site is surrounded by a dotted box in the left panel and zoomed in the right panel. Conserved RdRp motifs A–H and the priming loop are shown in bright orange, yellow, slightly green, cyan, violet, brown, magenta, dark grey and blue, respectively. **d**,**e**, The active sites of LACV (**d**) and FluA (**e**) polymerases upon vRNA promoter binding. **f**, Comparison of conformational differences in the active site between apo L (light grey) and 5′-hook-bound L (PDB ID: 8KI8). **g**, The hydrogen bond (dashed yellow lines) between C5 of the 5′ hook and Lys1291 of the fingertips stabilizes motif F (fingertips) of the polymerase active site. **h**,**i**, Interaction between motif F and 5′ hook RNA in LACV (**h**) and FluA (**i**) polymerases. **j**,**k**, Conservation analysis of amino acid Lys1291 in the polymerases of tospoviruses (**j**) and sNSVs (**k**). Identical residues are indicated with a red background, and similar residues are depicted in blue boxes with red text. A blue triangle highlights the position of Lys1291. **l**,**m**, Inoculation of *N. benthamiana* leaves with wild-type (WT) TSWV infectious clone (**l**) or its mutants (**m**), via agro-infiltration. Left panels of **l** and **m**, accumulation of eGFP fluorescence expressed from TSWV in *N. benthamiana* leaves was detected at 60 h post inoculation. Scale bars, 200 µm. Right panels of **l** and **m**, immunoblot analysis of eGFP and L protein expression in the leaves shown in the left panels was performed. M, medium segment; opt, codon-optimized; SR, small segment reporter; EV, empty vector. The RuBisCO large subunit was stained with Ponceau S (PS) to indicate sample loading.

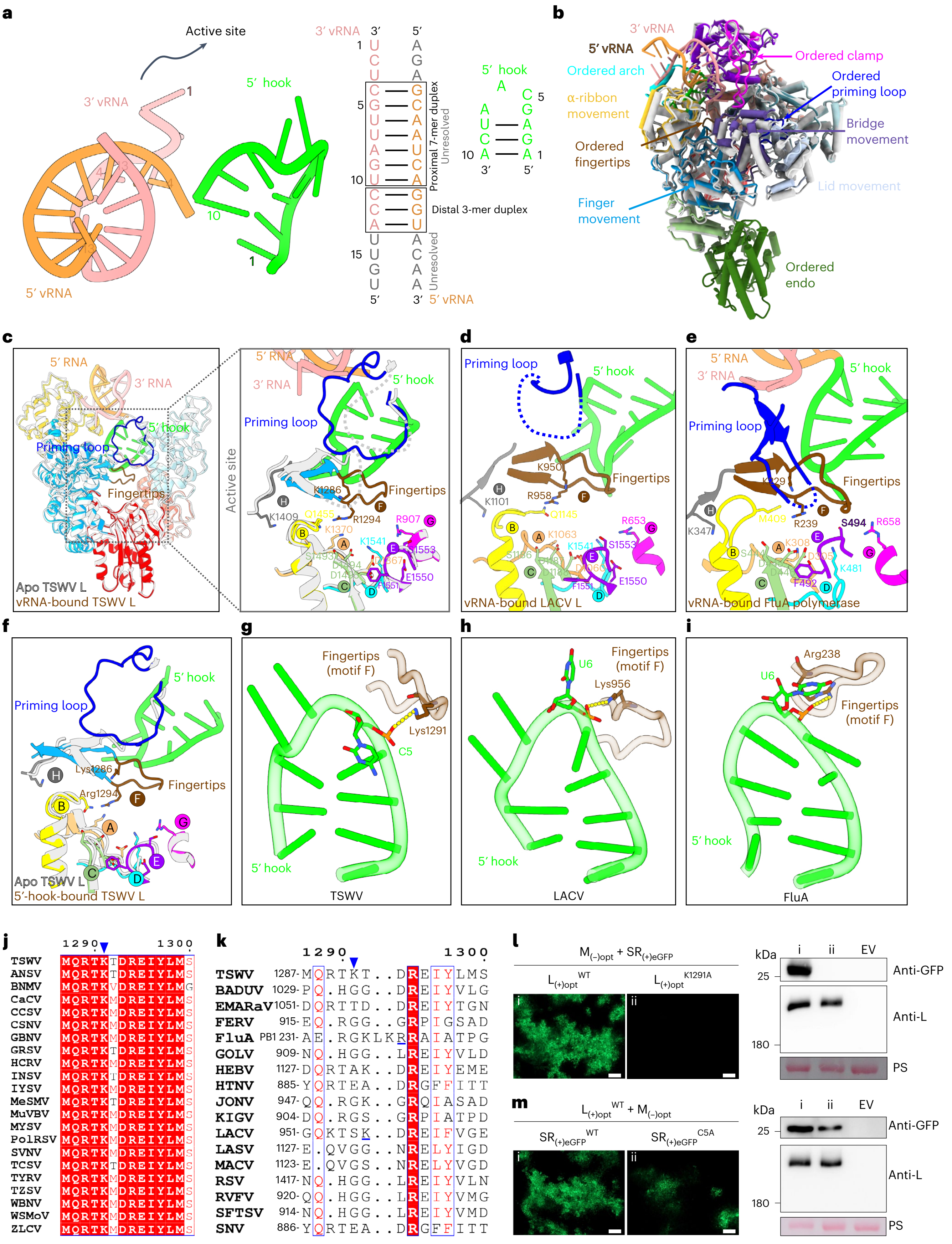
a
Active site
3′ vRNA
1
5′ hook
4
3
10
1
13
5′ vRNA
3′ vRNA 3′ 5′
1 U A
C G
U A
C — G
5 G — C
U — A
U — A
A — U
G — C
10 U — A
C — G
C — G
A — U
U A
15 U C
G A
U A
5′ 3′ 5′ vRNA
Proximal 7-mer duplex
Unresolved
Distal 3-mer duplex
Unresolved
5′ hook
A
C 5
A G
U — A
C — G
10 A — A 1
3′ 5′
b
3′ vRNA
5′ vRNA
Ordered arch
α-ribbon movement
Ordered fingertips
Finger movement
Ordered clamp
Ordered priming loop
Bridge movement
Lid movement
Ordered endo
c
5′ RNA
3′ RNA
5′ hook
Priming loop
Fingertips
Apo TSWV L
vRNA-bound TSWV L
5′ RNA
3′ RNA
5′ hook
Priming loop
Active site
K1286
Fingertips
H
K1409
Q1455
R1294
F
K1370
R907
G
A
B
K1541
S1553
S1493
E
D1494
S1367
E1550
D1495
C
F1551
D
d
Priming loop
5′ hook
K950
Fingertips
H
K1101
R958
F
Q1145
R653
G
B
A
K1063
K1541
S1553
S1186
E
D1188
C
E1550
F1551
D
vRNA-bound LACV L
e
5′ RNA
3′ RNA
5′ hook
Priming loop
Fingertips
K229
H
K347
F
M409
R239
S494
R658
E
B
A
K308
G
S444
D305
D446
K481
C
F492
D
vRNA-bound FluA polymerase
f
5′ hook
Priming loop
H
Lys1286
Fingertips
Arg1294
F
B
A
G
E
C
D
Apo TSWV L
5′-hook-bound TSWV L
g
Fingertips (motif F)
Lys1291
C5
5′ hook
TSWV
h
U6
Fingertips (motif F)
Lys956
5′ hook
LACV
i
Arg238
U6
Fingertips (motif F)
5′ hook
FluA
j
1290 1300
TSWV MQRTKTDREIYLMS
ANSV MQRTKTDREIYLMS
BNMV MQRTKVDREIYLMG
CaCV MQRTKMDREIYLMS
CCSV MQRTKMDREIYLMS
CSNV MQRTKMDREIYLMS
GBNV MQRTKMDREIYLMS
GRSV MQRTKTDREIYLMS
HCRV MQRTKMDREIYLMS
INSV MQRTKTDREIYLMS
IYSV MQRTKMDREIYLMS
MeSMV MQRTKTDREIYLMS
MuVBV MQRTKMDREIYLMS
MYSV MQRTKMDREIYLMS
PolRSV MQRTKMDREIYLMS
SVNV MQRTKMDREIYLMS
TCSV MQRTKTDREIYLMS
TYRV MQRTKMDREIYLMS
TZSV MQRTKMDREIYLMS
WBNV MQRTKMDREIYLMS
WSMoV MQRTKMDREIYLMS
ZLCV MQRTKMDREIYLMS
k
1290 1300
TSWV 1287- M Q R T K T . . D R E I Y L M S
BADUV 1029- P Q . H G G . . D R E I Y V L G
EMARaV 1051- D Q R T T D . . D R E I Y T G N
FERV 915- E Q . R G G . . G R P I G S A D
FluA PB1 231- A E . R G K L K R R A I A T P G
GOLV 909- N Q . H G G . . L R E I Y V L D
HEBV 1127- D Q R T A K . . D R E I Y E M E
HTNV 885- Y Q R T E A . . D R G F F I T T
JONV 947- Q Q . R G K . . G R Q I A S A D
KIGV 904- D Q . R G S . . G R P I A T P D
LACV 951- G Q K T S K . . D R E I F V G E
LASV 1127- E . Q V G G . . N R E L Y I G D
MACV 1123- E . Q V G S . . N R E L Y V G D
RSV 1417- N Q . H G G . . L R E I Y V L N
RVFV 920- Q Q . H G G . . L R E I Y V M G
SFTSV 914- N Q . H G G . . L R E I Y V M D
SNV 886- Y Q R T E A . . D R G F F I T T
l
$M_{(-)opt}$ + $SR_{(+)eGFP}$
$L_{(+)opt}^{WT}$
$L_{(+)opt}^{K1291A}$
i
ii
kDa
i ii EV
25
Anti-GFP
Anti-L
180
PS
m
$L_{(+)opt}^{WT}$ + $M_{(-)opt}$
$SR_{(+)eGFP}^{WT}$
$SR_{(+)eGFP}^{C5A}$
i
ii
kDa
i ii EV
25
Anti-GFP
Anti-L
180
PS

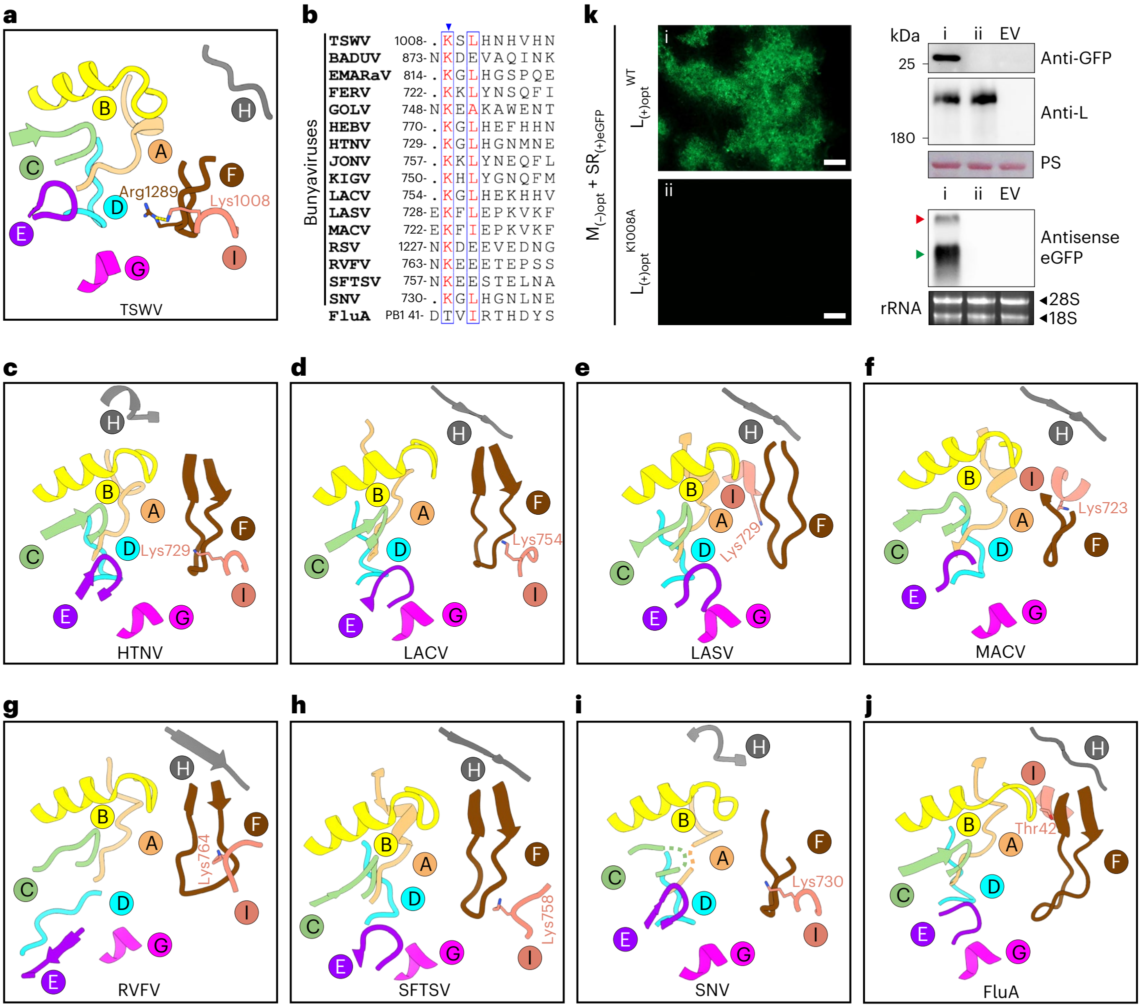

Fig. 3 | Newly identified conserved motif I in sNSV polymerases. a, Hydrogen bond (dashed yellow line) between Arg1289 of ordered fingertips and Lys1008 of the core lobe in the TSWV polymerase active site. **b**, The conservation of lysine (motif I) is shown in an alignment in bunyaviruses (TSWV (*Orthotospovirus*); BADUV, Badu virus (*Phasivirus*); EMARaV, European mountain ash ringspot-associated virus (*Emaravirus*); FERV, Ferak virus (*Orthoferavirus*); GOLV, Gouleako virus (*Goukovirus*); HEBV, Herbert virus (*Herbevirus*); HTNV (*Orthohnatavirus*); JONV, Jonchet virus (*Orthojonvirus*); KIGV, Kigluaik phantom virus (*Orthophasmavirus*); LACV (*Orthobunyavirus*); LASV (*Mammarenavirus*); MACV (*Mammarenavirus*); RSV, rice stripe virus (*Tenuivirus*); RVFV (*Phlebovirus*); SFTSV (*Phlebovirus*); SNV (*Orthohnatavirus*)) and orthomyxoviruses (FluA). The blue triangle highlights the position of the conserved lysine. **c**–**j**, The surroundings of motif I are illustrated for HTNV (**c**), LACV (**d**), LASV (**e**), MACV (**f**), RVFV (**g**), SFTSV (**h**), SNV (**i**) and FluA (**j**) with the neighbouring motifs A–H. **k**, *N. benthamiana* leaves were inoculated with wild-type TSWV infectious clone or its mutant via agro-infiltration. Accumulation of eGFP fluorescence expressed from rescued TSWV was detected in *N. benthamiana* leaves at 60 h post inoculation. Scale bars, 200 µm (left). Expression levels of eGFP, L and its mutant were analysed via western blot (top right), and the S genomic RNA (red arrowhead) and eGFP mRNA transcripts (green arrowhead) were analysed via northern blot using DIG-labelled antisense eGFP probes (bottom right). Ethidium bromide staining of ribosomal RNA (rRNA) was used as the RNA loading control.

end with nucleotides 11–13 of the 3′ end. Nucleotides 1–3 of the 5′ end are not visible, whereas nucleotides 1–3 of the 3′ end are visible and are directed towards the active sites of the polymerase (Fig. 2a). In addition, nucleotides 1–10 of the 5′ end form a stem–loop (‘hook’) in a hook-binding pocket. This structural arrangement primarily relies on a mismatched base pair (A1–A10) and two canonical base pairs (G2–C9 and A3–U8) (Fig. 2a).

The elucidation of the structure of L in its apo state allowed us to compare the conformational changes between vRNA-promoter-bound L and apo L. Superimposition of the two structures reveals a noticeable global rearrangement. The binding of the vRNA promoter (Supplementary Table 1) induces the movement of multiple subdomains, including the lid, bridge and α-ribbon, resulting in a more compact polymerase core and an ordered endo region (Fig. 2b). Furthermore, the vRNA promoter binding directly stabilizes the RNA-binding regions of TSWV L, including the arch and clamp domain (Fig. 2b). Two functional elements critical for enzyme activity, the fingertips (also known as motif F) and the priming loop, which are disordered in apo L, are stabilized in the vRNA-promoter-bound state (Fig. 2c). Similar to the vRNA-bound polymerases of LACV and FluA (Fig. 2d–e), the stabilized motif F, together with other motifs (motifs A–E, G and H), forms a stable catalytic centre.

5′ hook vRNA is sufficient to activate polymerase

Because nucleotides 1–10 of 5′-end vRNA form a special hook structure, we further prepared a complex of TSWV L and the single-stranded 5′ $\mathrm{vRNA}_{(1\text{–}10\ \mathrm{nts})}$ promoter and determined its structure to validate whether this hook structure alone can activate the L protein. The structure of the 5′-$\mathrm{vRNA}_{(1\text{–}10\ \mathrm{nts})}$–L complex was obtained at 3.2 Å (Extended Data Fig. 6a).

In 5′-$\mathrm{vRNA}_{(1\text{–}10\ \mathrm{nts})}$-bound L, both motif F and the priming loop are ordered compared with apo L and have a similar conformation to vRNA-promoter-bound L (Fig. 2f and Extended Data Fig. 6b), suggesting that the hook structure is sufficient to activate the L protein and facilitate the formation of the catalytic centre. The hydrogen bond between C5 of the 5′ end and residue Lys1291 of the fingertips plays a crucial role in the interaction between the RNA hook and motif F (Fig. 2g). Analysis of the interactions in other viral polymerase structures revealed that the residue Lys956 on motif F of the LACV L protein and the residue Arg238 on motif F of the FluA polymerase also form hydrogen bonds with the protruding base U6 at the bend of the hook structure (Fig. 2h,i). Moreover, residue Lys1291 is highly conserved among all orthotospovirus polymerases, but not those of animal viruses (Fig. 2j,k).

To further investigate the impact of the elements discerned in the activated L structure on viral replication, we introduced specific mutations in the TSWV infectious clone. More specifically, we mutated amino acid Lys1291 to Ala in the L segment and changed nucleotide C into A at the fifth position of the 5′ end in the S RNA template. Whereas clear fluorescence of the enhanced green fluorescent protein (eGFP) marker gene was observed in the agro-infiltrated leaves with wild-type TSWV at three days post inoculation (dpi), no fluorescence was observed with TSWV carrying the L^{K1291A} mutation (Fig. 2l). However, a significantly lower level of eGFP fluorescence was observed in the rescued TSWV containing the S^{C5A} mutation (Fig. 2m). The eGFP accumulation and production of L protein in each sample was verified by immunoblotting and indicated that the mutation introduced into the L protein had no significant effect on its stability (Fig. 2l,m). We also mutated other amino acid residues (Tyr455, Lys467, Thr468, Thr653, Lys656, Asp775, Arg823, Pro824, Gln825, Arg826, Leu827, Arg831, Thr895, Lys896, Leu897, Val1014, His1015, Thr1018, Lys1191, and Glu1432) in the L protein that interact with hook RNA in the viral infectious clone and found that all of them are essential for the rescue of TSWV (Extended Data Fig. 7).

Formation of a complete catalytic centre

To investigate how the ordered motif F functions, we further analysed the interaction between motif F and other regions of the TSWV L protein. Motif F is primarily involved in direct polar interactions with the fingers and core lobe regions, including hydrogen bond interaction between conserved residue Arg1294 and conserved residue Gln1455 on motif B (Fig. 3a and Supplementary Table 2). Also, residue Arg1289 interacts with residue Lys1008, which we found to be absolutely conserved in the L proteins of all bunyaviruses; we denoted this area as motif I (Fig. 3a,b).

To verify the spatial position of motif I in the polymerase structures of other sNSVs, we analysed the active sites of all structurally resolved polymerases. As shown in Fig. 4c–j, motif I is consistently observed in the polymerase active site across various viruses. In traditional bunyaviruses such as HTNV, LACV, RVFV, SFTSV, SNV and TSWV, the conserved Lys residue resides on a flexible loop, proximal to both motif F and motif G (Fig. 3c,d,g–i). For arenaviruses (newly classified in the order Bunyavirales), including LASV and MACV, the conserved Lys residue is located on an α-helix and is close to motif A, motif H and motif F (Fig. 3e,f). In the case of FluA, the spatial characteristics of the Thr42 amino acid are similar to those of arenaviruses (Fig. 3j), indicating that motif I in influenza viruses and arenaviruses may be evolutionarily closer.

To explore the biological role of motif I, we evaluated the effect of the residue Lys1008 on virus replication using TSWV infectious clones. Wild-type and mutant-infected clones were infiltrated into *Nicotiana benthamiana* leaves. eGFP fluorescence was observed in leaves infiltrated with the wild type at 3 dpi, but no fluorescence was observed in leaves infiltrated with the clone carrying the L^{K1008A} mutation (Fig. 3k). Protein immunoblot analysis indicated that both wild-type and mutant L protein were expressed normally, and the accumulation of eGFP protein was consistent with fluorescence intensity (Fig. 3k). These results confirm the crucial role of Lys1008 in rescuing the virus.

Dual-targeted inhibition of polymerase activation

Currently, there are no chemical antiviral compounds directly targeting plant viruses. The structural similarities between the RdRp structure of TSWV and those of the animal/human-infecting viruses of the Bunyavirales and influenza viruses suggest that human antiviral drugs targeting RdRp may also be effective against TSWV. To test this, we used the TSWV infectious clones to screen the inhibitory effects of three well-known human antiviral drugs—namely, remdesivir, ribavirin and favipiravir—on viral replication. Infectious clones were co-infiltrated with the drugs in *N. benthamiana* leaves, and eGFP fluorescence was examined at 3 dpi. Leaves treated with remdesivir revealed a significant reduction in eGFP expression, while leaves treated with ribavirin showed no fluorescence, indicating that both drugs, in particular ribavirin, were effective against TSWV replication (Extended Data Fig. 8). Although a small amount of fluorescence was observed in the leaves treated with favipiravir, the leaves exhibited necrosis, indicating potential phytotoxicity.

To further substantiate these findings, we also tested the effect of ribavirin on a normal viral infection. *N. benthamiana* leaves were mechanically inoculated with TSWV in the absence (buffer control) and presence of a ribavirin solution at a concentration of 100 μg ml^{-1}. In the buffer-control-treated group, typical symptoms of a viral infection, including leaf curling and stunting, were observed in the systemic (newly emerged) leaves at 14 and 21 dpi. The presence of TSWV in the systemic leaves was confirmed by immunoblotting assays from as early as 7 dpi. In contrast, in the ribavirin-treated group, no typical symptoms of viral infection were observed in the systemic leaves at any time point, and the absence of TSWV in ribavirin-treated plants was confirmed by immunoblotting (Fig. 4a). These findings indicate that ribavirin strongly inhibits TSWV infection, which is consistent with previous reports[37,38]. Given that ribavirin is a nucleoside analogue, we hypothesized that its antiviral activity may be attributed to its interaction with the TSWV polymerase, potentially disrupting viral genomic RNA synthesis. To investigate this and identify the binding site of the nucleoside analogue, we mixed purified TSWV polymerase with ribavirin and determined the complex structure at atomic resolution (Supplementary Fig. 6).

Fig. 4 | Mechanism of TSWV inhibition by ribavirin. a, Effects of ribavirin treatment on TSWV infection. *N. benthamiana* plants inoculated with TSWV were subjected to treatment with either buffer or ribavirin (100 μg ml^{-1}). Left: disease development was photographed at 7, 14 and 21 dpi. Right: the accumulation level of nucleocapsid protein (NP) in the systemic leaves of treated plants was determined via immunoblot analysis using an NP-specific antibody. CK+, TSWV-infected sample. **b**, Left: cut-away global view of the L-ribavirin complex (PDB ID: 8KI6). The upper right panel provides a close-up and sliced-surface view of ribavirin located in the middle of the 5′-hook-binding pocket and the template-binding channel. The lower right panel offers a magnified view of ribavirin positioned in the active site. Ribavirin is shown as a blue shape. **c**, vRNA structures within the 5′-hook-binding pocket and template-binding channel of the L–ribavirin complex, achieved by superimposing the vRNA-bound L structure onto the ribavirin-bound L structure described here. The two surface views display the location of ribavirin in vRNA-binding position. **d**, Illustration of the entrance and exit tunnels and active site of L depicting how ribavirin inhibits activity of the polymerase. The L structure (grey) with vRNA (coloured) is displayed with tunnels (cyan) labelled with arrows as template entry, NTP entry, product and template exit tunnel, as calculated using Caver v.3.0.3 (left). Ribavirin is superimposed on the same tunnels as in the left panel and is depicted in blue (right). **e**, 5′ hook RNA binding analysis of the L protein in the absence or presence of ribavirin by EMSA. Increasing concentrations of L protein were incubated with FAM-labelled 5′ hook $RNA_{(1-10\ nts)}$ in the absence of ribavirin (lanes 1–4), and the L and FAM-labelled 5′ hook RNA mixtures were incubated with decreasing amounts of ribavirin (lanes 5–8). **f**, Effect of ribavirin on in vitro RNA synthesis directed by TSWV RNP. Digoxin-labelled RNA synthesized in vitro by heat-inactivated virus (lane 2) and untreated virus in the absence (lane 1) and presence (lanes 3–5) of increasing concentrations of ribavirin (25, 50 and 100 μg ml^{-1}, respectively).

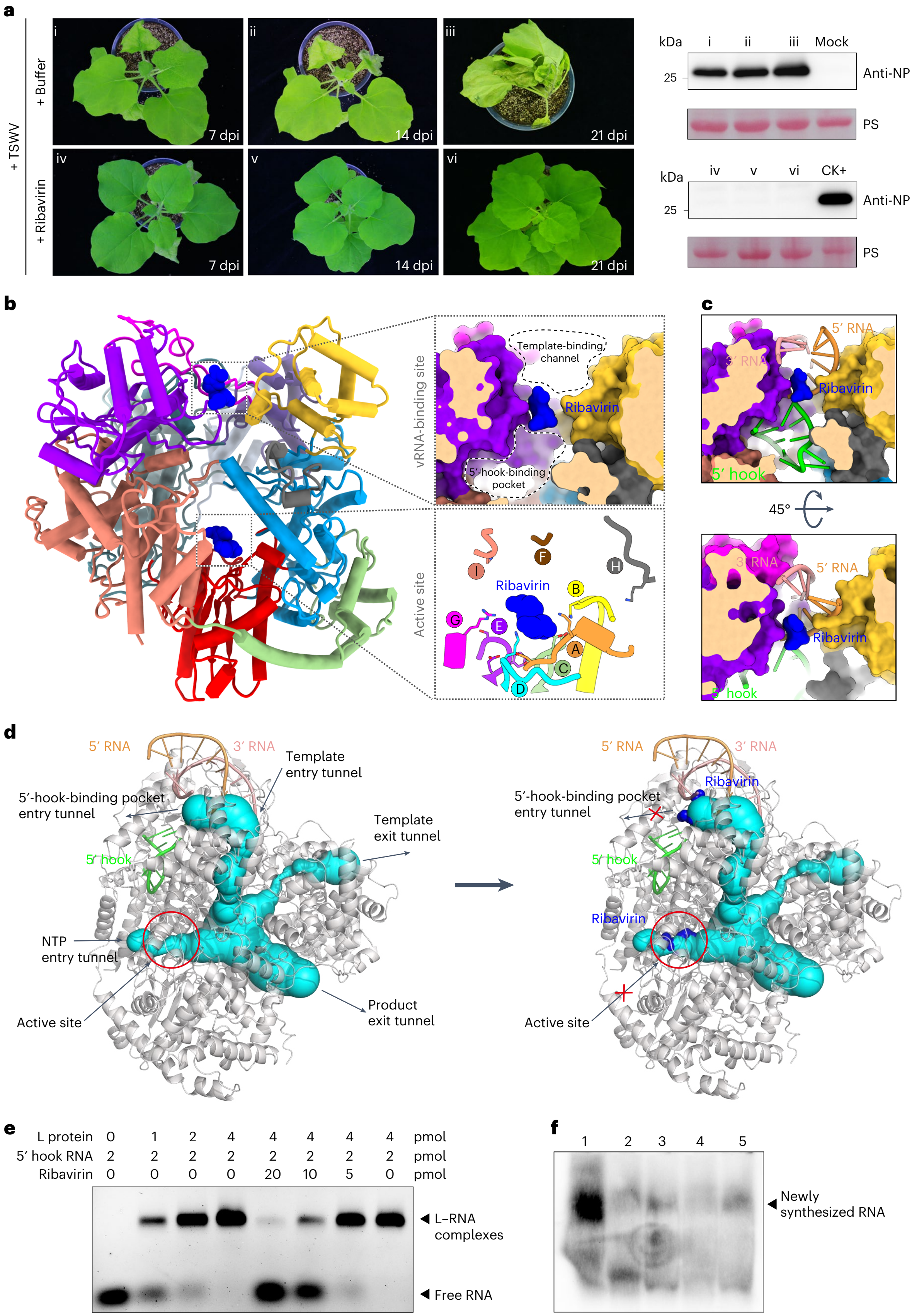
a
+ TSWV
+ Buffer
+ Ribavirin
i
ii
iii
iv
v
vi
7 dpi
14 dpi
21 dpi
kDa
i ii iii Mock
25
Anti-NP
PS
kDa
iv v vi CK+
25
Anti-NP
PS
b
vRNA-binding site
Template-binding channel
Ribavirin
5′-hook-binding pocket
Active site
Ribavirin
A
B
C
D
E
F
G
H
I
c
5′ RNA
3′ RNA
Ribavirin
5′ hook
45°
3′ RNA
5′ RNA
Ribavirin
5′ hook
d
5′ RNA
3′ RNA
Template entry tunnel
5′-hook-binding pocket entry tunnel
5′ hook
Template exit tunnel
NTP entry tunnel
Active site
Product exit tunnel
5′ RNA
3′ RNA
Ribavirin
5′-hook-binding pocket entry tunnel
5′ hook
Ribavirin
Active site
e
L protein 0 1 2 4 4 4 4 4 pmol
5′ hook RNA 2 2 2 2 2 2 2 2 pmol
Ribavirin 0 0 0 0 20 10 5 0 pmol
L–RNA complexes
Free RNA
f
1 2 3 4 5
Newly synthesized RNA

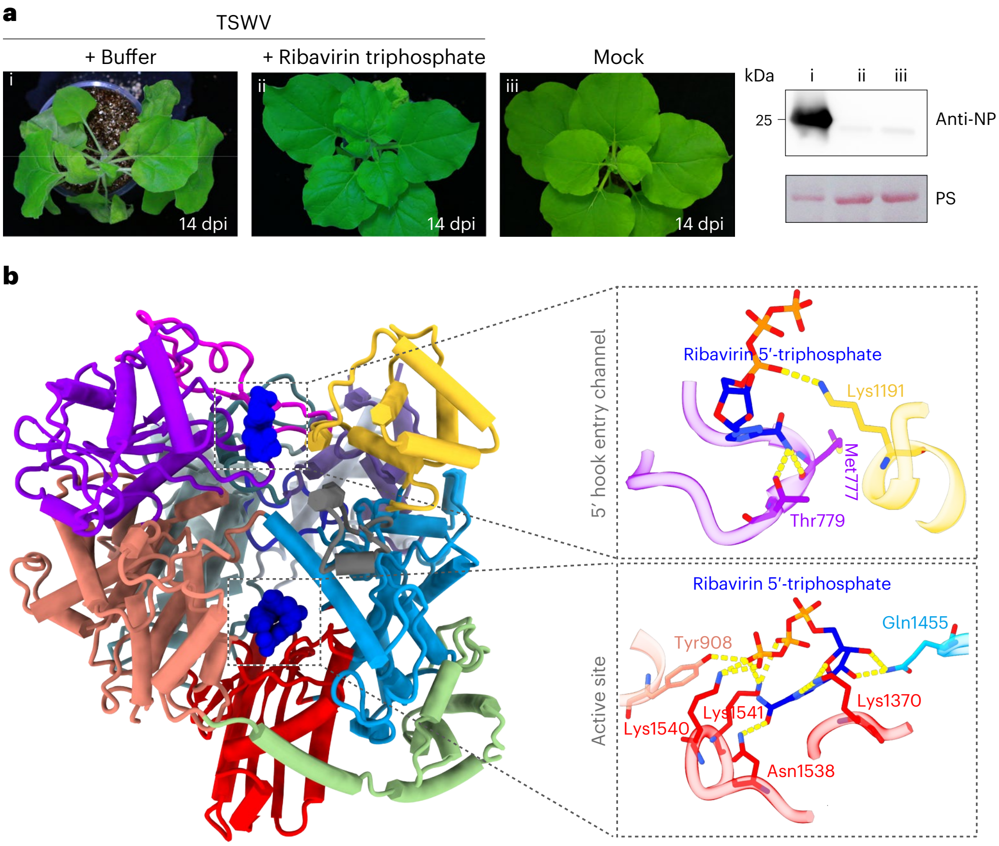

Fig. 5 | The inhibition of TSWV L by ribavirin triphosphate. a, Effects of ribavirin triphosphate treatment on TSWV infection. *N. benthamiana* plants inoculated with TSWV were subjected to treatment with either buffer or ribavirin triphosphate (100 μg ml^{-1}). Left: disease development was photographed at 14 dpi. Right: the accumulation level of TSWV NP protein in the systemic leaves of treated plants was determined via immunoblot analysis using an NP-protein-specific antibody. Ponceau S staining of the RuBisCO large subunit was used to indicate sample loading. **b**, Left: cut-away global view of the TSWV L–ribavirin triphosphate complex (PDB ID: 9J8V). The L protein is coloured by domain with the same colour code as in Fig. 1. Ribavirin triphosphate is represented as a blue shape with a dashed outline. The right panel shows detailed interactions between L and ribavirin triphosphate. The hydrogen bonds are shown as yellow dashed lines.

Unexpectedly, compared with the density map of L protein in the apo state, the complex revealed two additional densities for L–ribavirin (Supplementary Fig. 7), indicating that ribavirin targets two sites on TSWV L. Ribavirin binds not only to the active site of the polymerase but also to a key channel located in the RNA-binding site (Fig. 4b). By modelling the viral promoter structure in the complex and calculating the internal tunnel of the L core, we found that ribavirin occupies two key sites that effectively block both the active catalytic formation and the entry of the 5′ end into the hook-binding pocket required for the formation of a stem–loop (hook) structure (Fig. 4c,d). Given the previously mentioned critical role of the hook structure in activating the L protein, ribavirin binding at this channel position prevents the allosteric activation of polymerase.

We also performed an electrophoretic mobility shift assay (EMSA) to investigate the binding affinity change between the L protein and 5′ hook RNA in the presence or absence of ribavirin. As shown in Fig. 4e, a fixed amount of FAM (fluorescein)-labelled 5′ hook RNA (1.5 pmol) was incubated with increasing concentrations of TSWV L protein. The free RNA probe was able to completely shift in the presence of 4 pmol of L protein. Upon the addition of ribavirin, RNA shift was significantly reduced, suggesting that ribavirin is able to prevent the L protein from binding 5′ hook RNA (Fig. 4e). Furthermore, we investigated the inhibition activity of ribavirin by an in vitro RdRp activity experiment as reported in ref. 39. Purified TSWV ribonucleoprotein complex (RNP) was incubated in the presence of NTPs (including digoxin-labelled UTP) to synthesize RNA in vitro. The digoxin-labelled RNA synthesized in vitro by heat-inactivated TSWV RNP and untreated RNP in the absence and presence of ribavirin were resolved by RNA gel electrophoresis and further analysed by northern blot. High amounts of RNA product were observed in the absence of ribavirin, while the total amount of RNA synthesis was decreased considerably in the presence of ribavirin (Fig. 4f). These data suggest that ribavirin can inhibit the RNA synthesis activity of polymerase in vitro.

Because ribavirin is a prodrug, it would be activated by intracellular phosphorylation into mono-, di- and triphosphates. The inhibition mechanism of ribavirin against TSWV in *N. benthamiana* leaves may depend on the activated form of ribavirin. We further tested the effect of ribavirin triphosphate treatment on TSWV infection in planta. *N. benthamiana* leaves were mechanically inoculated with TSWV in the absence (buffer control) and presence of a ribavirin triphosphate solution at a concentration of 100 μg ml^{-1}. Typical symptoms of viral infection were observed in the buffer-control-treated plants, whereas no typical symptoms appeared in the ribavirin-triphosphate-treated plants at 14 dpi (Fig. 5a). These data suggest that ribavirin triphosphate also strongly inhibits TSWV infection. In addition, we prepared a complex of TSWV L and ribavirin triphosphate and determined its structure at 3.0 Å (Supplementary Fig. 8). Similar to the dual-target binding pattern of ribavirin on TSWV L protein, ribavirin triphosphate binds to both the active site of the polymerase and the entry channel of 5′ hook RNA. Ribavirin triphosphate located in the entry channel forms hydrogen bonds with residues Lys1191, Met777 and Thr779, while active-site-located ribavirin triphosphate makes

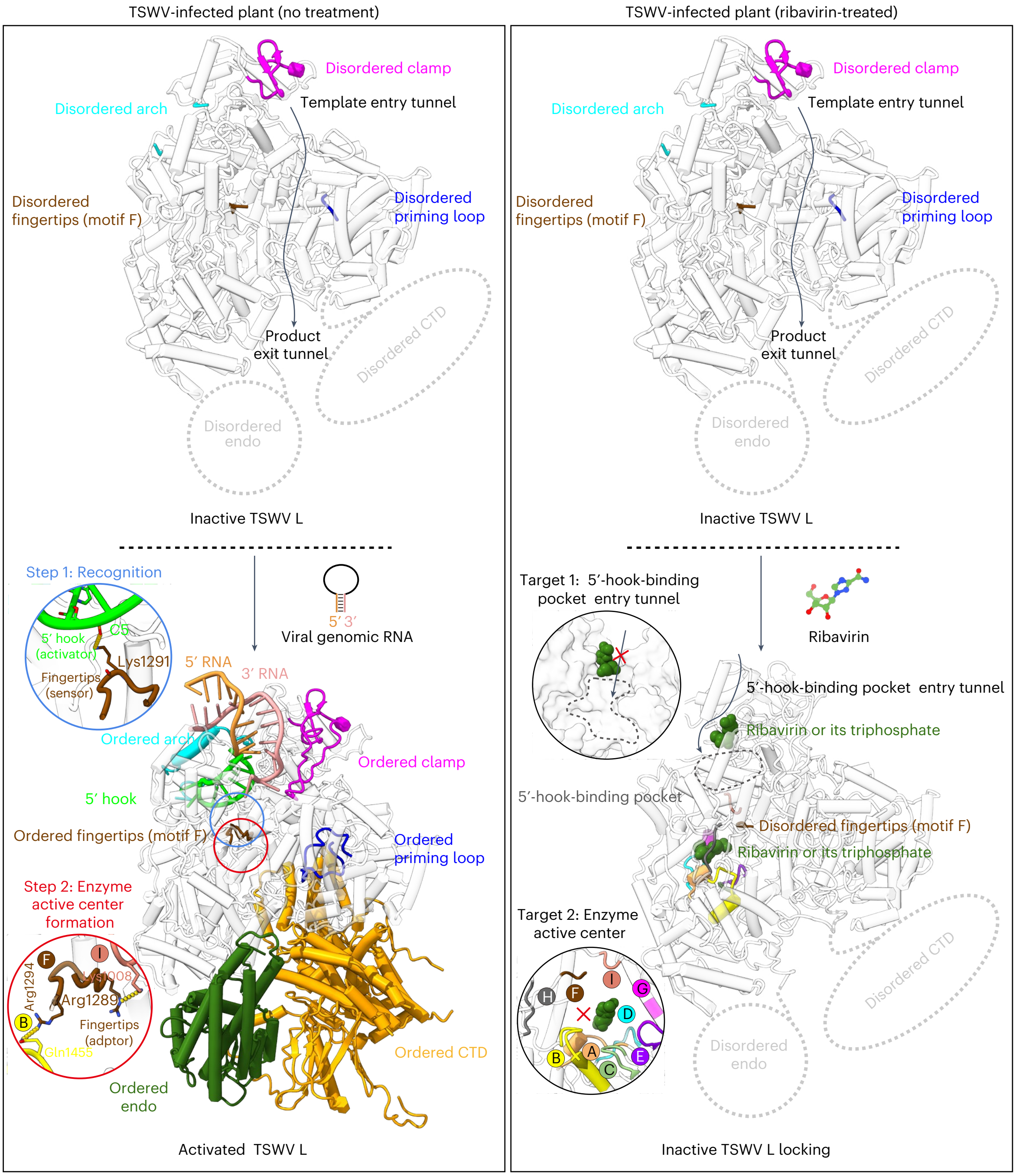

Fig. 6 | Structure-based model of TSWV L activation and its dual-targeted inhibition mechanisms. In TSWV-infected plants, the newly synthesized L protein (apo L) remains in an inactivated state with a disordered active site. When the viral genome with a double-stranded terminus binds to the L protein, the proximal double strand unwinds; the 3′ end becomes single-stranded and enters the polymerase active centre, and nucleotides 1–10 of the 5′ end enter the hook-binding pocket to form a hook-like stem–loop. The protruding base C5 at the bend of the hook structure makes hydrogen bonds with Lys1291 of the fingertips (motif F), resulting in an ordered motif F. New hydrogen bonds (Arg1294–Gln1455 and Arg1289–Lys1008) between motif F and other motifs contribute to the formation of a complete polymerase active centre. These alterations in the active site together with the ordered endo and CTD engage TSWV L in an activated state to initiate replication and transcription processes. In ribavirin-treated plants, ribavirin or its triphosphate disrupts both vRNA recognition and the formation of a complete catalytic centre by occupying both the 5′-hook-binding pocket entry tunnel and the enzyme's active centre, locking the polymerase in an inactivated state.

hydrogen bonds with Tyr908, Lys1540, Lys1541, Asn1538, Lys1370 and Gln1455 (Fig. 5b).

Discussion

The structure of TSWV L reported here reveals the structural features of an RNA polymerase from a plant virus belonging to the sNSVs with commonalities to animal-infecting viruses. Polymerases from picornavirus to influenza virus typically range from ~50 to 250 kDa; therefore, the ~330-kDa TSWV L represents the largest polymerase in terms of molecular weight among all resolved RNA polymerase structures to date. The overall architecture of the TSWV L protein consists of three main components: the N-terminal endo fusing a metal-binding protein-like domain, the central core region containing the RdRp polymerase and the variable CTD comprising the cap-binding domain region

(Fig. 1 and Extended Data Fig. 1). This implies a common evolutionary origin between plant and animal RNA polymerases of sNSVs. RNA polymerases larger than TSWV L (for example, the ~450-kDa Nairovirus L protein) may also have a similar overall architecture.

The structure of the viral promoter has been controversial in the literature, with various models such as the 'panhandle', 'fork', 'corkscrew' or 'hook' proposed on the basis of structural and functional studies of influenza viruses[40]. The current paradigm of sNSVs polymerase structures is that the vRNA promoter binds to the polymerase in a hook structure, supported by the presence of a stem–loop (hook) structure formed by the 5′ proximal strand and a distal duplex formed by the 5′ and 3′ distal strands[5]. However, it is still unclear whether proximal 5′ and 3′ single-stranded RNA ends can form a proximal duplex and assemble into a panhandle-like structure. The two single-stranded terminal ends of viral genomic elements, making up the panhandle structure and comprising the promoter of bunyaviruses, are more complementary than those of influenza virus[6]. In this study, we observed a proximal double-stranded region formed in the viral promoter on the TSWV L protein (Figs. 1c and 2a) that is not observed in influenza virus, whereas a distal duplex is observed in both influenza virus and bunyavirus polymerases[8,11,14,20,21,24] (Extended Data Fig. 5). Although the presence of a duplex consisting of the proximal nucleotides 1–10 of the 5′ end with the 3′ end and simultaneous formation of a hook structure in the 5′ end is not an actual state, it still reveals the possibility of the vRNA promoter binding in a fully double-stranded conformation at the template entrance channel of the polymerase. We propose that the newly synthesized L protein (apo L) in TSWV-infected plants is in an inactive state and initially binds to genomic RNA with a fully double-stranded end (Figs. 2a and 6). The binding of the vRNA promoter allows the 5′ end to enter the hook-binding pocket, where it folds into a stabilized hook structure and simultaneously activates the polymerase's active site, together with ordered endo and CTD to engage it in replication and transcription processes (Figs. 1 and 6). Upon treatment of TSWV-infected plants with ribavirin, ribavirin or its triphosphate form binds to both the 5′-hook-binding pocket entry tunnel and the enzyme's active site, blocking both vRNA recognition and the formation of a complete catalytic centre, two key steps in polymerase activation, and ultimately locking the polymerase in an inactivated state (Figs. 4–6).

A set of eight structural motifs (A to H) of RdRp play a key role in catalysing RNA synthesis. Motif F comprises positively charged residues that interact with the phosphate group of incoming NTP. Through the interactions between positively charged residues on motif F and nucleotides on the hook RNA in TSWV polymerase (Fig. 2g), another potential role of motif F emerges—it might function as a 'sensor' to detect the unique hook structure formed by viral genomic RNA. This recognition is a critical step for polymerase activation. Furthermore, to our knowledge, no new motifs have been reported since the identification of two previously unknown conserved motifs, G and H, specific to all sNSV polymerases by Gerlach et al. in 2015[14]. In this study, while analysing the intramolecular interaction of the TSWV L protein with motif F, we unexpectedly discovered an absolutely conserved lysine in the bunyavirus L protein (Fig. 3a,b). Further structural alignment revealed that this conserved lysine is present in the active site of all sNSV polymerases (Fig. 4c–j), indicating the identification of a new motif, denoted I, which provides deeper insights into the composition of the active site of the sNSV polymerases. Following the recognition of vRNA by the disordered motif F, the region becomes ordered, taking on the role of an 'adaptor', and generates new interactions with other residues (including motif I), thereby placing the polymerase in an activated state. Moreover, the Lys1008 residue makes an ionic contact with the product strand phosphate group at the +3 position from the active site when we model a duplex RNA into the active site. This traps the tip of the motif F finger sequence underneath itself, fully structuring motif F for NTP binding and activity (Extended Data Fig. 9). Therefore, another key mechanistic insight may be that this ordering of motif F is probably dependent on first making a ≥3-base-pair product RNA to establish the Lys1008–phosphate contact, and this may in turn trigger a transition to a stable elongation complex.

In contrast to the rapid development of agricultural fungicides, insecticides and herbicides, there remains a notable gap in antiviral pesticides. To investigate the occurrence of similar interactions between viral polymerases and ribavirin or its triphosphate, we searched the PDB database and found structures of ribavirin complexes with the polymerases of noroviruses and aphthoviruses[41,42], both of which are positive-stranded RNA viruses. In these structures, ribavirin or its triphosphate binds to a single target site within the catalytic core of the polymerase (Extended Data Fig. 10). The structures of the TSWV L–ribavirin and TSWV L–ribavirin triphosphate complexes thus reveal unique dual target sites of the antiviral nucleoside analogue. In addition to occupying the active site, they can bind at the 5′-hook-binding pocket entry tunnel of TSWV L, preventing the 5′ end from entering the hook-binding pocket to form a hook structure to activate the polymerase (Fig. 4b–d).

Because the components of human and veterinary drugs are now banned from use as pesticides to avoid the emerging risk of resistance, ribavirin is not currently available for direct application to crops, and therefore plant-virus-specific drugs need to be developed. Considering that interaction between the Lys amino acid at position 1291 of the L protein and the C base at the fifth position of the 5′ end hook is crucial for viral infection and is highly conserved in orthotospoviruses but not conserved in human and animal sNSVs (Fig. 2j,k), the Lys1291–C5 interaction site could serve as a specific target for designing pesticides against plant orthotospoviruses. In addition, since the formation of the 5′ end hook structure is a common feature in the initiation stage of sNSV polymerases, the polymerase hook formation tunnel presents a highly attractive target for the design of broad-spectrum antiviral drugs against sNSVs.

Methods

Protein expression and purification

The codon-optimized sequence for the L protein (GenBank: JF960237.1) of the TSWV-YN isolate was synthesized and cloned into a pFastBac expression plasmid with an N-terminal 10×His–Msyb tag. Recombinant baculoviruses were prepared using SF9 insect cells (11496015, Invitrogen), and protein expression was carried out in High Five cells (B85502, Invitrogen) via the Bac-to-Bac expression system. At 60 h post inoculation, the culture was centrifuged to pellet the cells, which were subsequently resuspended in chilled lysis buffer (50 mM Tris (pH 8.0), 200 mM NaCl, 10 mM imidazole) and then lysed by sonication. After centrifugation at 14,000 *g* for 1 h at 4 °C, the supernatant was loaded twice onto a Ni-affinity column (GE) pre-equilibrated with lysis buffer. The resin was washed three times with 120 ml of lysis buffer, and the bound proteins were eluted with elution buffer containing imidazole (50 mM Tris (pH 8.0), 200 mM NaCl, 300 mM imidazole) and then captured onto a 5-ml Q column (GE Healthcare). The proteins bound to the column were eluted with a linear concentration gradient of NaCl, and the fractions that peaked at 380 mM NaCl were pooled together. Subsequently, this pooled fraction was loaded onto a Superose 6 10/300 GL column (GE Healthcare) and eluted in 50 mM Tris (pH 8.0), 200 mM NaCl, 1 mM Tris (2-carboxyethyl) phosphine buffer. The sample in the single peak was concentrated, flash-frozen and stored at −80 °C before use.

Cryo-EM sample preparation and data collection

Purified TSWV L protein was concentrated to 1.2 mg ml^{-1} for sample preparation. L protein was mixed with (1) 5′ vRNA$_{(1–17\,\mathrm{nts})}$ 5′-pAGAGCA AUCAGGUACAA-3′ OH) and 3′ vRNA$_{(1–17\,\mathrm{nts})}$ (5′-pUGUUACCUGAU UGCUCU-3′ OH), (2) 5′ vRNA$_{(1–10\,\mathrm{nts})}$ (5′-pAGAGCAAUCA-3′OH), (3) ribavirin or (4) ribavirin 5′-triphosphate at a 1:1.5 molar ratio and incubated for 5 min on ice. Holy-carbon gold grid (Cflat R1.2/1.3

mesh 300) was freshly glow-discharged with a Solarus 950 plasma cleaner (Gatan) for 30 s. A 3-µl aliquot of the complex was transferred onto the grids, blotted with filter paper at 22 °C and 100% humidity, and plunged into ethane using a Vitrobot Mark IV (FEI). For the apo L and L–5′-vRNA$_{(1\text{-}17\ \mathrm{nts})}$–3′-vRNA$_{(1\text{-}17\ \mathrm{nts})}$ complex, micrographs were collected at 300 kV using a Titan Krios microscope (Thermo Fisher), equipped with a K2 detector (Gatan), using SerialEM automated data collection software[43]. Videos (32 frames, every 0.2 s, total dose 60 e− Å^{-2}) were recorded at a final pixel size of 1.04 Å with a defocus of between −1.5 and −2.0 µm. For the L–5′-vRNA$_{(1\text{-}10\ \mathrm{nts})}$ and L–ribavirin complexes, micrographs were collected at 300 kV using a Titan Krios microscope (Thermo Fisher), equipped with a K3 detector (Gatan), using SerialEM automated data collection software[43]. Videos (32 frames, every 0.2 s, total dose 60 e− Å^{-2}) were recorded at a final pixel size of 1.07 Å with a defocus of between −1.5 and −2.0 µm. For the L–ribavirin triphosphate complex, micrographs were collected at 300 kV using a Titan Krios microscope (Thermo Fisher), equipped with a Falcon4 detector (Gatan), using SerialEM automated data collection software[43]. Videos (32 frames, every 0.2 s, total dose 60 e− Å^{-2}) were recorded at a final pixel size of 1.07 Å with a defocus of between −1.5 and −2.0 µm.

Image processing

For the apo L, L–5′-vRNA$_{(1\text{–}17\ \mathrm{nts})}$–3′-vRNA$_{(1\text{–}17\ \mathrm{nts})}$ complex, L–5′-vRNA$_{(1\text{–}10\ \mathrm{nts})}$, L–ribavirin complex and L–ribavirin 5′-triphosphate complex, a total of 4,135, 4,557, 4,109, 3,659 and 3,853 micrographs were recorded, respectively. An almost equivalent image processing strategy was used for all the datasets. First, the raw data were processed using MotionCor2 by aligning them and averaging them into motion-corrected summed images. After that, the defocus value for each micrograph was determined using Gctf[44]. Next, micrographs of high quality were selected for further processing. Particles were then picked and extracted for two-dimensional alignment[45]. Well-defined particles were selected from here for initial model reconstruction. The initial model was used as a reference for 3D classification. After refinement and post-processing, the overall resolution of the TSWV L apo state, L–5′3′-vRNA, L–5′-vRNA, L–ribavirin and L–ribavirin triphosphate was up to 3.9 Å, 3.7 Å, 3.2 Å, 3.4 Å and 3.0 Å, respectively, on the basis of the gold-standard Fourier shell correlation (threshold, 0.143)[46]. The quality of the local resolution was evaluated using ResMap[47]. In L–5′-vRNA datasets, the CTD of L was observed. Among the five 3D classes, the subset, making up 4% of total particles, displayed clear features of the CTD in L. After refinement and post-processing, the overall resolution of TSWV L containing the CTD improved to 4.0 Å. In addition, local refinement and DeepEMhancer were used for further improving the quality of the CTD map[48].

Model building and refinement

The initial structure model was built using the AutoBuild program in Phenix and further corrected manually by real-space refinement in COOT v.1.1.11. An AlphaFold model comprising the CTD region was used to guide the model building in COOT of parts of the CTD (in areas where the map density was present but its quality was too low for ab initio unambiguous building).

Infectious clones and virus inoculation

The *Agrobacterium tumefaciens* culture carrying the full-length TSWV infectious clone L$_{(+)\mathrm{opt}}$, M$_{(-)\mathrm{opt}}$ and SR$_{(+)\mathrm{eGFP}}$ was obtained from a previously reported source[49]. For virus inoculation, *N. benthamiana* leaf tissues infected with the virus were ground at a ratio of 1:10 (w/v) in a 0.01 M phosphate buffer solution at pH 7.0. The resulting crude leaf extracts were then used for rub-inoculation onto the leaves of *N. benthamiana* plants. The inoculated tobacco plants were cultivated in a growth chamber under day/night temperatures of 23 °C/25 °C, with a photoperiod of 16 h of light and 8 h of darkness.

Antiviral drug treatment of plant leaves

To prepare 100 µg ml^{-1} solutions of remdesivir (SF1193-5MG, Beyotime), ribavirin (R9644-10MG, Sigma-Aldrich), ribavirin 5′-triphosphate (sc-358826, Santa Cruz Biotechnology) and favipiravir (PHR9070-50MG, Sigma-Aldrich), 1 mg of powder of each of these drugs was mixed with 200 µl of DMSO solvent separately. After the solids were completely dissolved, 10 ml of ddH$_2$O (containing 1% Tween-20) was added to formulate the solution. One hour post inoculation of the *N. benthamiana* leaves with the virus, solutions containing the drug were evenly applied to the surface of the leaves by a brush.

Fluorescence microscopy

N. benthamiana leaves were collected between 24 and 72 h post agro-infiltration, and GFP fluorescence was assessed using an inverted fluorescence microscope (IX-71-F22 FL/DIC; Olympus). GFP was excited at 488 nm, and the emitted fluorescence was collected through a GFP barrier filter (Olympus). Images were captured and analysed with Image-Pro software (Olympus).

Immunoblots

Total protein was extracted from 1.0 g of agro-infiltrated *N. benthamiana* leaf tissue in 2 ml of extraction buffer containing 10% (v/v) glycerol, 25 mM Tris-HCl (pH 7.5), 1 mM EDTA, 150 mM NaCl, 10 mM dithiothreitol, 2% (w/v) polyvinylpolypyrrolidone, 0.5% (v/v) Triton X-100 and 1× protease inhibitor cocktail. Protein samples were separated on SDS–PAGE gels, transferred to PVDF membranes, blocked with a 5% skim milk solution and then incubated with primary antibodies, such as anti-GFP (1:5,000, Sigma-Aldrich), anti-TSWV L (1:500, lab-made) and anti-TSWV NP (1:10,000, lab-made)) at room temperature for 2 h or overnight at 4 °C. After incubation with a secondary antibody, such as HRP-conjugated goat anti-rabbit (1:10,000, Sigma-Aldrich) or goat anti-mouse (1:10,000, Sigma-Aldrich), for 1 h, the blots were detected using the ECL Substrate Kit (Thermo Scientific).

Total RNA extraction and northern blotting analysis

Total RNA was extracted from *N. benthamiana* plant leaves using a Total RNA Purification Kit from Tiangen. For northern blot analysis, specific DIG-labelled probes for both sense and antisense eGFP were synthesized using a DIG High Prime RNA labelling kit from Roche. Total RNAs were separated on 1% formaldehyde agarose gels and then transferred to Hybond-N+ membranes from GE Healthcare. The membrane blots were subsequently hybridized with the specific DIG-labelled probe and processed following the manufacturer's protocol using a DIG-High Prime Detection Starter Kit II, also from Roche.

EMSA

In a standard EMSA, varying amounts of L protein were incubated in 10 µl of binding buffer (45 mM Tris, 45 mM boric acid, pH 8.4) along with 1.5 pmol of FAM-labelled RNA probe (GenScript). The reaction mixtures were incubated at room temperature for 10 min, followed by the addition of 5 µl of loading buffer (0.1% bromophenol blue, 0.1% xylene cyanol and 15% Ficoll 400 in 0.5× TBE buffer). The mixtures were then separated by electrophoresis on a 1.5% agarose gel in 0.5× TBE buffer (45 mM Tris, 45 mM boric acid, 1 mM EDTA, pH 8.0). The gel was subsequently electroblotted onto a nylon membrane (Hybond N+; GE Healthcare). The FAM-labelled RNA was detected using ChemiDoc Imaging Systems from BioRad.

In vitro TSWV RdRp activity assay

In vitro RdRp assays were performed as described in ref. 39, with minor modifications. The assays used 10–15 µg of purified TSWV RNP in a final volume of 25 µl, containing 20 mM HEPES (pH 7.4), 0.5 mM magnesium acetate, 5 mM MnCl$_2$, 2.5 mM DTT, 1 mM of each NTP (including digoxin-labelled UTP, 53119620, Roche), 0.1% NP-40 and 0.8 U µl^{-1} RNasin. The reaction mixtures were incubated at 30 °C for

1.5 h. Digoxin-labelled RNA products were separated by electrophoresis on a 1.0% agarose gel, followed by downward northern blotting.

Statistics and reproducibility

All biological analysis experiments were performed in triplicates.

Reporting summary

Further information on research design is available in the Nature Portfolio Reporting Summary linked to this article.

Data availability

All data associated with this study are presented in the paper or the Supplementary Information and can also be obtained from the corresponding authors upon request. The cryo-EM maps and atomic models have been deposited at the Electron Microscopy Data Bank and the Protein Data Bank with accession codes EMDB 37256 and PDB 8KIA (TSWV L apo state), EMDB 37253 and PDB 8KI7 (TSWV L–5′3′-vRNA), EMDB 37254 and PDB 8KI8 (TSWV L–5′-vRNA), EMDB 37255 and PDB 8KI9 (TSWV L containing CTD), EMDB 37252 and PDB 8KI6 (TSWV L–ribavirin bound), and EMDB 61241 and PDB 9J8V (TSWV L–ribavirin triphosphate bound). Additional details regarding each dataset can be found in Supplementary Tables 3 and 4. Source data are provided with this paper.

References

1. Lomonossoff, G. P. So what have plant viruses ever done for virology and molecular biology? *Adv. Virus Res.* **100**, 145–162 (2018).
2. Harrison, B. D. A brief outline of the development of plant virology in the 20th century. *J. Plant Pathol.* **91**, 509–520 (2009).
3. Jones, R. A. C. & Naidu, R. A. Global dimensions of plant virus diseases: current status and future perspectives. *Annu. Rev. Virol.* **6**, 387–409 (2019).
4. Tatineni, S. & Hein, G. L. Plant viruses of agricultural importance: current and future perspectives of virus disease management strategies. *Phytopathology* **113**, 117–141 (2023).
5. te Velthuis, A. J. W., Grimes, J. M. & Fodor, E. Structural insights into RNA polymerases of negative-sense RNA viruses. *Nat. Rev. Microbiol.* **19**, 303–318 (2021).
6. Malet, H., Williams, H. M., Cusack, S. & Rosenthal, M. The mechanism of genome replication and transcription in bunyaviruses. *PLoS Pathog.* **19**, e1011060 (2023).
7. Takashita, E. Influenza polymerase inhibitors: mechanisms of action and resistance. *Cold Spring Harb. Perspect. Med.* **11**, a038687 (2021).
8. Pflug, A., Guilligay, D., Reich, S. & Cusack, S. Structure of influenza A polymerase bound to the viral RNA promoter. *Nature* **516**, 355–360 (2014).
9. Reich, S. et al. Structural insight into cap-snatching and RNA synthesis by influenza polymerase. *Nature* **516**, 361–366 (2014).
10. Peng, Q. et al. Structural insight into RNA synthesis by influenza D polymerase. *Nat. Microbiol.* **4**, 1750–1759 (2019).
11. Fan, H. et al. Structures of influenza A virus RNA polymerase offer insight into viral genome replication. *Nature* **573**, 287–290 (2019).
12. Hengrung, N. et al. Crystal structure of the RNA-dependent RNA polymerase from influenza C virus. *Nature* **527**, 114–117 (2015).
13. Wandzik, J. M. et al. A structure-based model for the complete transcription cycle of influenza polymerase. *Cell* **181**, 877–893 (2020).
14. Gerlach, P., Malet, H., Cusack, S. & Reguera, J. Structural insights into bunyavirus replication and its regulation by the vRNA promoter. *Cell* **161**, 1267–1279 (2015).
15. Arragain, B. et al. Pre-initiation and elongation structures of full-length La Crosse virus polymerase reveal functionally important conformational changes. *Nat. Commun.* **11**, 3590 (2020).
16. Arragain, B. et al. Structural snapshots of La Crosse virus polymerase reveal the mechanisms underlying Peribunyaviridae replication and transcription. *Nat. Commun.* **13**, 902 (2022).
17. Wang, X. et al. Structure of Rift Valley fever virus RNA-dependent RNA polymerase. *J. Virol.* **96**, e0171321 (2022).
18. Wang, P. P. et al. Structure of severe fever with thrombocytopenia syndrome virus L protein elucidates the mechanisms of viral transcription initiation. *Nat. Microbiol.* **5**, 864–871 (2020).
19. Vogel, D. et al. Structural and functional characterization of the severe fever with thrombocytopenia syndrome virus L protein. *Nucleic Acids Res.* **48**, 5749–5765 (2020).
20. Williams, H. M. et al. Structural insights into viral genome replication by the severe fever with thrombocytopenia syndrome virus L protein. *Nucleic Acids Res.* **51**, 1424–1442 (2023).
21. Trouilleton, Q. D., Barata-Garcia, S., Arragain, B., Reguera, J. & Malet, H. Structures of active Hantaan virus polymerase uncover the mechanisms of Hantaviridae genome replication. *Nat. Commun.* **14**, 2954 (2023).
22. Durieux Trouilleton, Q., Housset, D., Tarillon, P., Arragain, B. & Malet, H. Structural characterization of the oligomerization of full-length Hantaan virus polymerase into symmetric dimers and hexamers. *Nat. Commun.* **15**, 2256 (2024).
23. Meier, K. et al. Structural and functional characterization of the Sin Nombre virus L protein. *PLoS Pathog.* **19**, e1011533 (2023).
24. Peng, R. C. et al. Structural insight into arenavirus replication machinery. *Nature* **579**, 615–619 (2020).
25. Kang, H. L. et al. Structural basis for recognition and regulation of arenavirus polymerase L by Z protein. *Nat. Commun.* **12**, 4134 (2021).
26. Kouba, T. et al. Conformational changes in Lassa virus L protein associated with promoter binding and RNA synthesis activity. *Nat. Commun.* **12**, 7018 (2021).
27. Xu, X. et al. Cryo-EM structures of Lassa and Machupo virus polymerases complexed with cognate regulatory Z proteins identify targets for antivirals. *Nat. Microbiol.* **6**, 921–931 (2021).
28. Scholthof, K. B. G. et al. Top 10 plant viruses in molecular plant pathology. *Mol. Plant Pathol.* **12**, 938–954 (2011).
29. Turina, M., Kormelink, R. & Resende, R. O. Resistance to tospoviruses in vegetable crops: epidemiological and molecular aspects. *Annu. Rev. Phytopathol.* **54**, 347–371 (2016).
30. Zhu, M., van Grinsven, I. L., Kormelink, R. & Tao, X. Paving the way to tospovirus infection: multilined interplays with plant innate immunity. *Annu. Rev. Phytopathol.* **57**, 41–62 (2019).
31. Kormelink, R., Verchot, J., Tao, X. & Desbiez, C. The Bunyavirales: the plant-infecting counterparts. *Viruses* **13**, 842 (2021).
32. Thompson, A. A. & Peersen, O. B. Structural basis for proteolysis-dependent activation of the poliovirus RNA-dependent RNA polymerase. *EMBO J.* **23**, 3462–3471 (2004).
33. Ferrer-Orta, C. et al. Structure of foot-and-mouth disease virus RNA-dependent RNA polymerase and its complex with a template-primer RNA. *J. Biol. Chem.* **279**, 47212–47221 (2004).
34. Lu, G. L. & Gong, P. Crystal structure of the full-length Japanese encephalitis virus NS5 reveals a conserved methyltransferase–polymerase interface. *PLoS Pathog.* **9**, e1003549 (2013).
35. Liang, B. et al. Structure of the L protein of vesicular stomatitis virus from electron cryomicroscopy. *Cell* **162**, 314–327 (2015).
36. Holm, L. DALI and the persistence of protein shape. *Protein Sci.* **29**, 128–140 (2020).
37. De Fazio, G., Caner, J. & Vicente, M. Effect of virazole (ribavirin) on tomato spotted wilt virus in two systemic hosts, tomato and tobacco. *Arch. Virol.* **63**, 305–309 (1980).
38. Liu, Q., Zhao, C., Sun, K., Deng, Y. & Li, Z. Engineered biocontainable RNA virus vectors for non-transgenic genome editing across crop species and genotypes. *Mol. Plant* **16**, 616–631 (2023).

39. van Knippenberg, I., Goldbach, R. & Kormelink, R. Purified particles support both genome replication and transcription. *Virology* **303**, 278–286 (2002).
40. Ferhadian, D. et al. Structural and functional motifs in influenza virus RNAs. *Front. Microbiol.* **9**, 559 (2018).
41. Ferrer-Orta, C. et al. Sequential structures provide insights into the fidelity of RNA replication. *Proc. Natl Acad. Sci. USA* **104**, 9463–9468 (2007).
42. Alam, I. et al. Crystal structures of murine norovirus-1 RNA-dependent RNA polymerase in complex with 2-thiouridine or ribavirin. *Virology* **426**, 143–151 (2012).
43. Mastronarde, D. N. Automated electron microscope tomography using robust prediction of specimen movements. *J. Struct. Biol.* **152**, 36–51 (2005).
44. Zhang, K. Gctf: real-time CTF determination and correction. *J. Struct. Biol.* **193**, 1–12 (2016).
45. Scheres, S. H. Processing of structurally heterogeneous cryo-EM data in RELION. *Methods Enzymol.* **579**, 125–157 (2016).
46. Scheres, S. H. & Chen, S. Prevention of overfitting in cryo-EM structure determination. *Nat. Methods* **9**, 853–854 (2012).
47. Kucukelbir, A., Sigworth, F. J. & Tagare, H. D. Quantifying the local resolution of cryo-EM density maps. *Nat. Methods* **11**, 63–65 (2014).
48. Sanchez-Garcia, R. et al. DeepEMhancer: a deep learning solution for cryo-EM volume post-processing. *Commun. Biol.* **4**, 874 (2021).
49. Feng, M. F. et al. Rescue of tomato spotted wilt virus entirely from complementary DNA clones. *Proc. Natl Acad. Sci. USA* **117**, 1181–1190 (2020).

Acknowledgements

We thank X. Huang, B. Zhu, X. Li and L. Chen for cryo-EM data collection at the Center for Biological Imaging in the Institution of Biophysics, CAS. This work was supported by the National Natural Science Foundation of China (grant numbers 32170162, 32472516 to J.L. and 31925032, 32220103008 and 32430088 to X.T.), the Jiangsu Key Technology R&D Program and International Science and Technology Cooperation Project (grant number BZ2023030 to X.T.), the Independent Innovation of Agricultural Science and Technology of Jiangsu Province (grant number CX [22] 2039 to X.T.) and the Guidance Foundation, the Sanya Institute of Nanjing Agricultural University (grant number NAUSY-MS19 to X.T.), the Young Elite Scientists Sponsorship Program by CAST (grant number 2022QNRC001 to L.C.) and the Youth Innovation Promotion Association of CAS grant to L.C.

Author contributions

X.T. and X.W. conceived and conceptualized the study. J.L., L.C., Y.Z., J.S., L.W. and M.F. performed the experiments. J.L. and L.C. analysed the data. J.L., L.C., X.T. and X.W. interpreted the results. J.L. and L.C. wrote the initial drafts of the paper. M.Z., Y.Y. and R.K. made critical comments on paper writing. X.W. and X.T. revised the paper.

Competing interests

The authors declare no competing interests.

Additional information

Extended data is available for this paper at https://doi.org/10.1038/s41477-025-01940-y.

Supplementary information The online version contains supplementary material available at https://doi.org/10.1038/s41477-025-01940-y.

Correspondence and requests for materials should be addressed to Xiaorong Tao or Xiangxi Wang.

Peer review information *Nature Plants* thanks Yi Shi and the other, anonymous, reviewer(s) for their contribution to the peer review of this work.

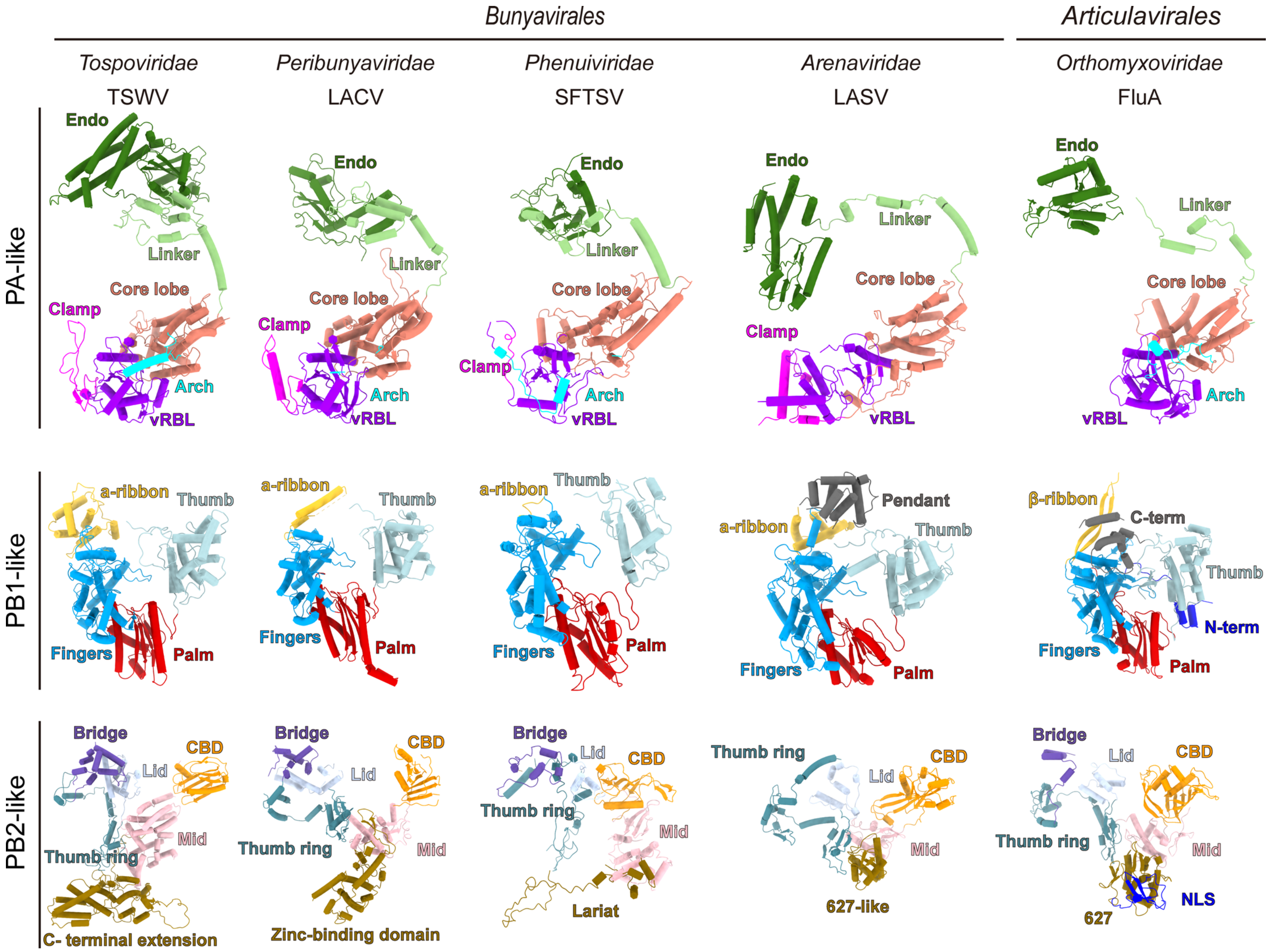

Extended Data Fig. 1 | Structural comparison of individual domains among sNSV polymerases. Viral polymerases with complete structure including TSWV L, LACV L (PDB ID: 6Z6G), SFTSV L (PDB ID: 6L42), LASV L (PDB ID: 7OJN) and FluA polymerase (PDB ID: 4WSB) are shown as ribbon. PA-like (upper panel), PB1-like (middle panel) and PB2-like (lower panel) domain between these polymerases all share a similar overall architecture. For TSWV L, more α-helix structures than other polymerases are present in the endo region and α-ribbon region, respectively. The separated regions in PB2-like domain are relatively variable, except for the structurally conserved CBD region.

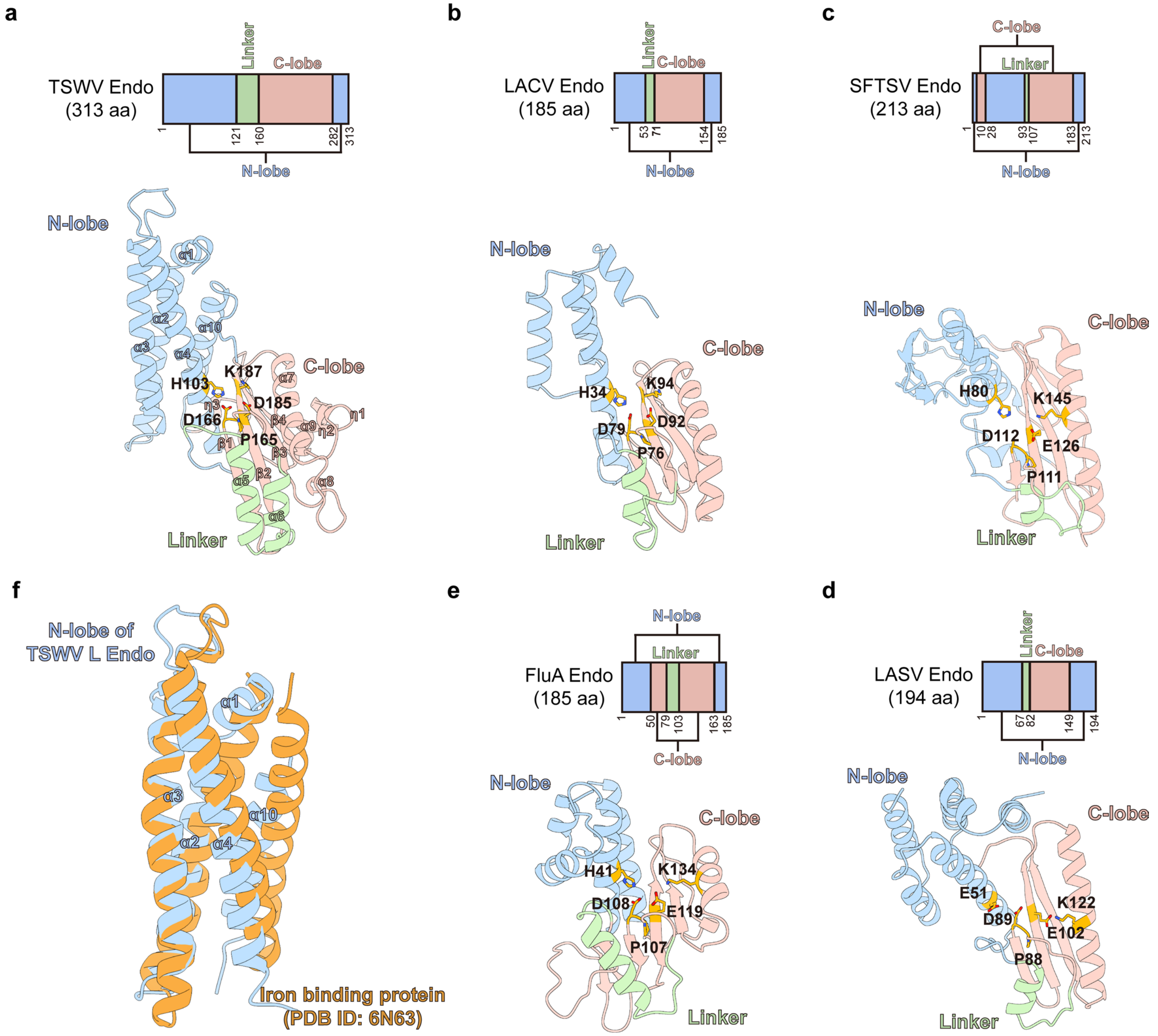

Extended Data Fig. 2 | Structural comparison of sNSV L Endonucleases. Endonuclease region of TSWV L (**a**), LACV L (**b**), SFTSV L (**c**), LASV L (**d**) and FluA polymerase (**e**): schematic representation (top) and structure (bottom). Corresponding structural elements are presented in the same color. The side chains of the key motif that constitute the active site are displayed as orange sticks. f, N-lobe of TSWV endo and an iron binding protein (PDB ID: 6N63) exhibit a remarkably high degree of structural similarity.

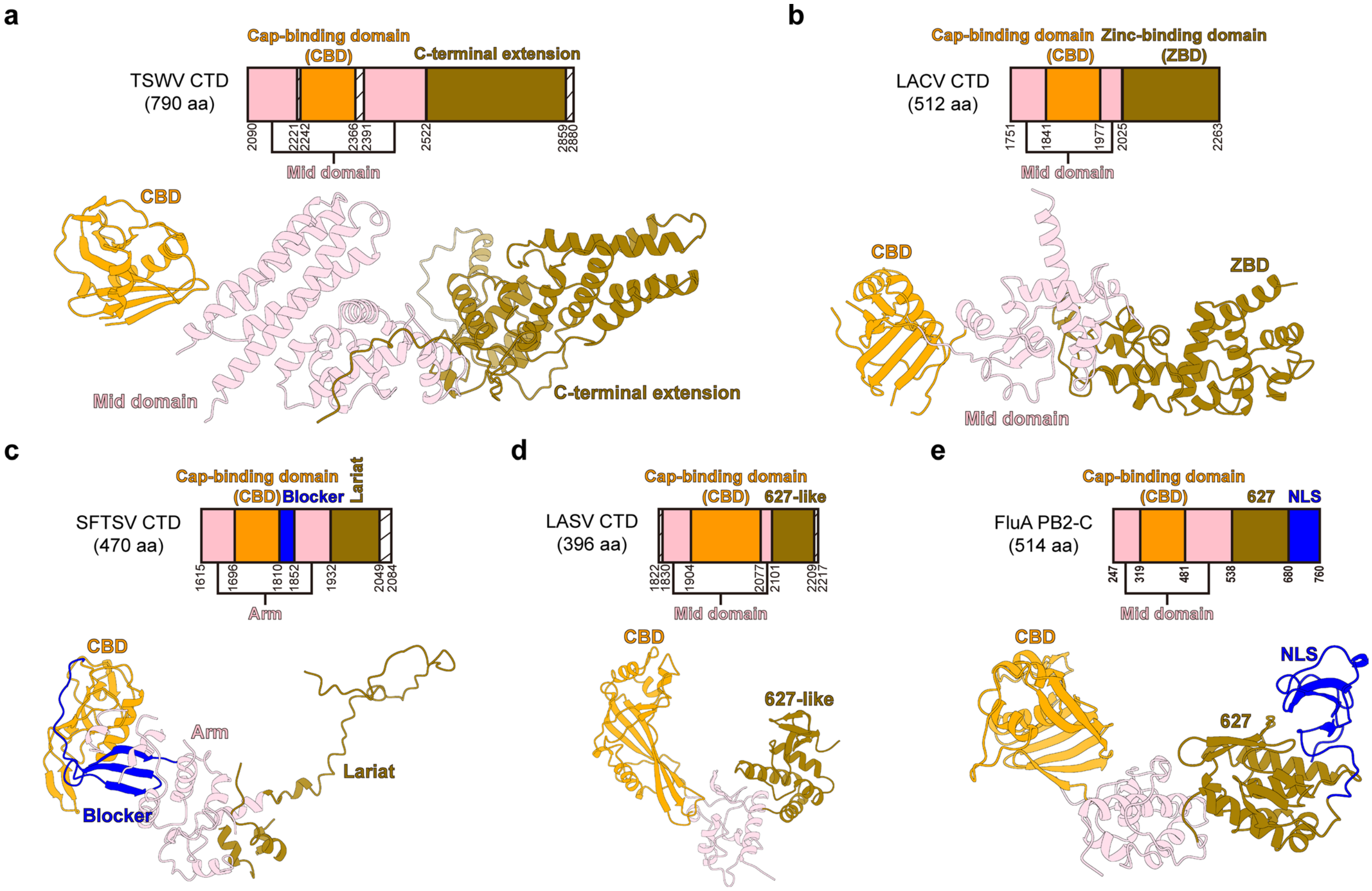

Extended Data Fig. 3 | Structural comparison of CTD domain of TSWV L, LACV L, SFTSV L, LASV L and FluA polymerase. a–e, Schematic representation (top) and structure (bottom). Similar domains are displayed in the same color.

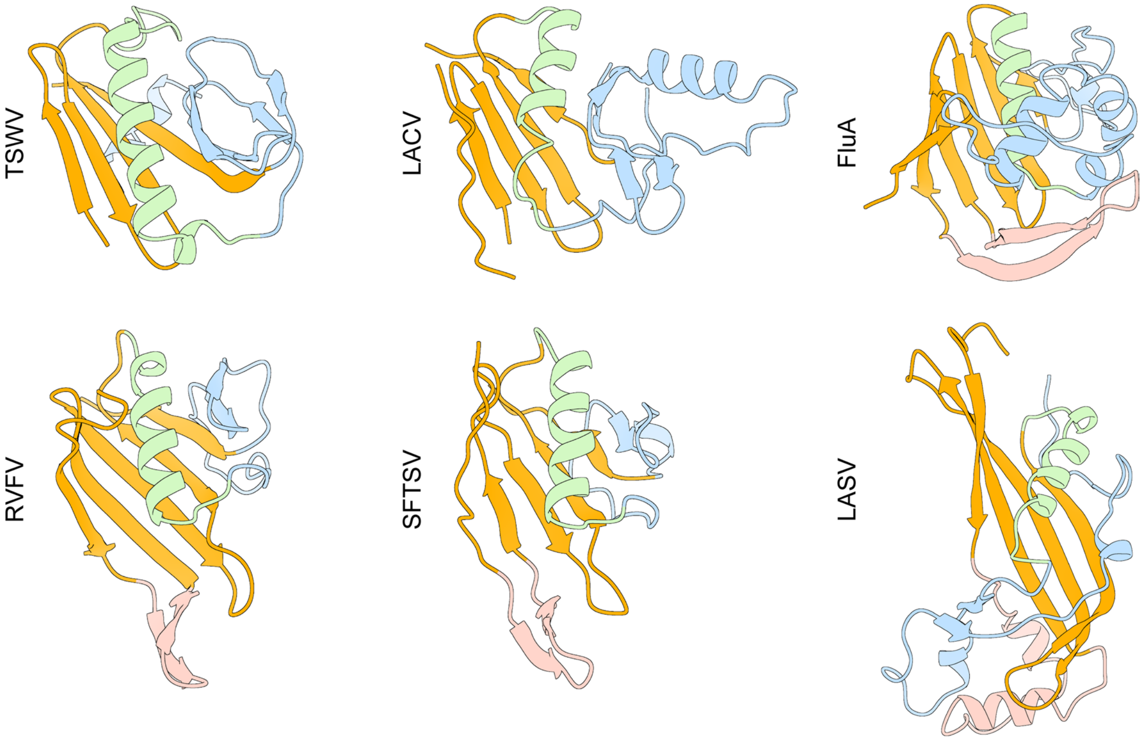

Extended Data Fig. 4 | Structural comparison of CBD domain between sNSV polymerases. Alignment of the structures of TSWV L, LACV L, RVFV L (PDB ID: 6QHG), SFTSV L, LASV L and FluA polymerase CBD domain in the same orientation. Similar structure elements are colored in the same way.

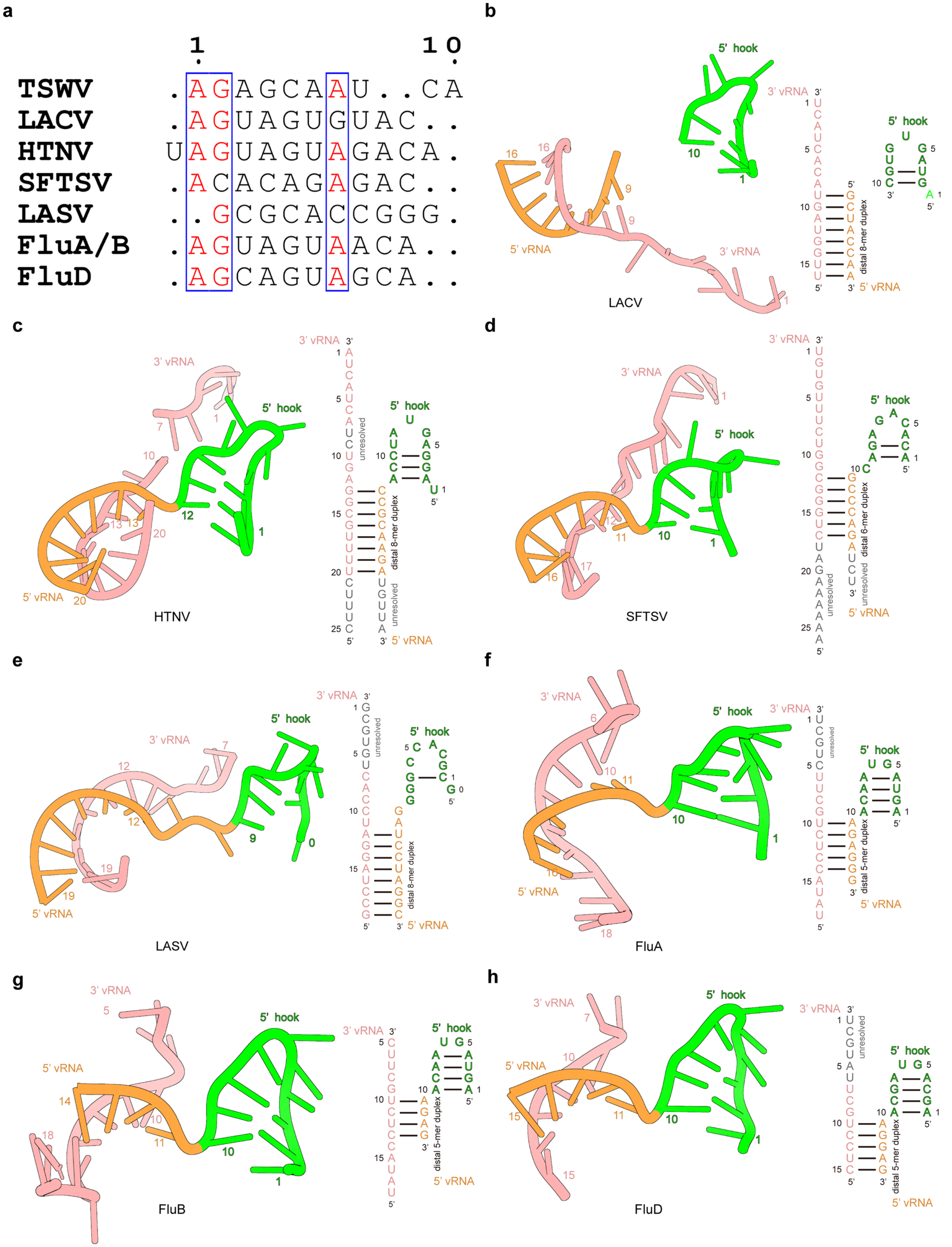

Extended Data Fig. 5 | Comparison of vRNA promotors. **a**, Alignment of the 5′ hook sequences from TSWV, LACV, HTNV, SFTSV, LASV, and FluA/B/D genomic RNAs was generated using ClustalW and visualized with ESPript. Similar residues are coloured red in blue boxes. **b-h**, The vRNA promoters of TSWV, LACV, SFTSV, LASV, and FluA/B/D polymerases are presented in both structural (left) and schematic (right) representations. RNA nucleotides that are present but not visible are shown in gray. The canonical base pairings between nucleotides are indicated with lines.

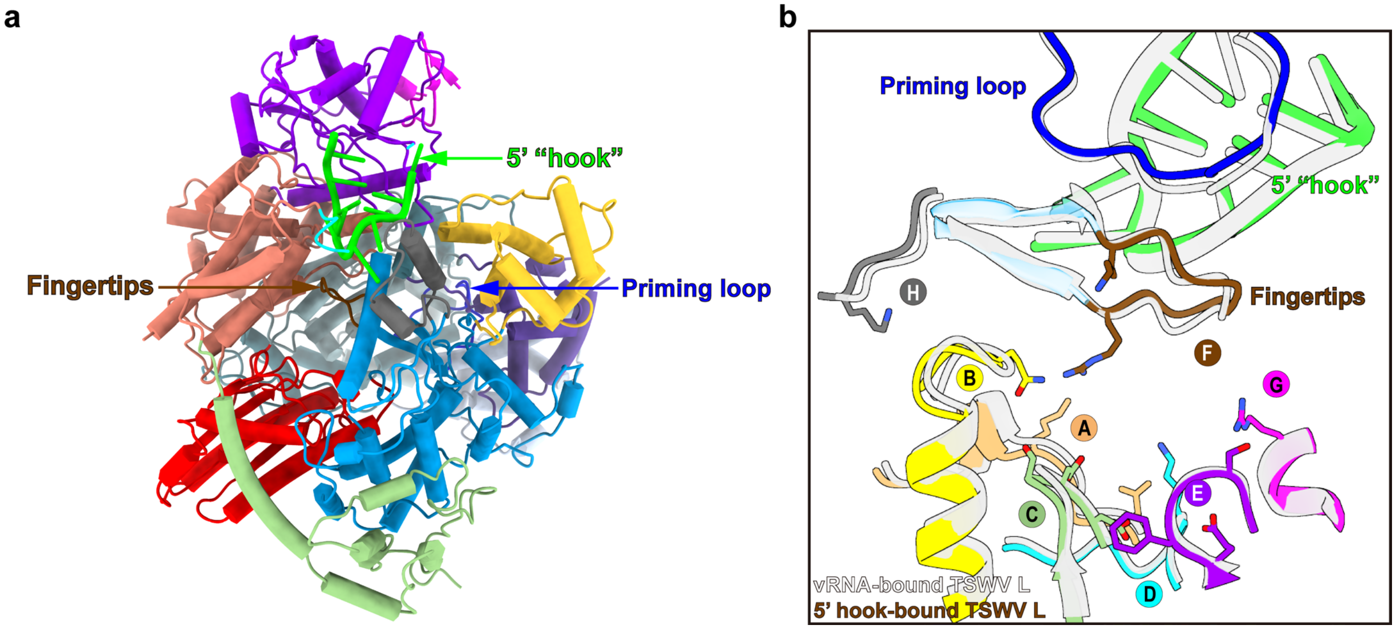

Extended Data Fig. 6 | The active site structure of 5′ hook-bound and vRNA-bound TSWV L share similar characteristics. a, Overall structure of the TSWV-L complex with 5′ hook. The L-5′ hook complex is displayed in cartoon representation with the same colors as in Fig. 1. **b**, Structural comparison of the active site between 5′ hook-bound L (colored) and 5′_3′ vRNA promoter-bound L (light grey). The motifs and priming loop are shown and colored as in Fig. 2c.

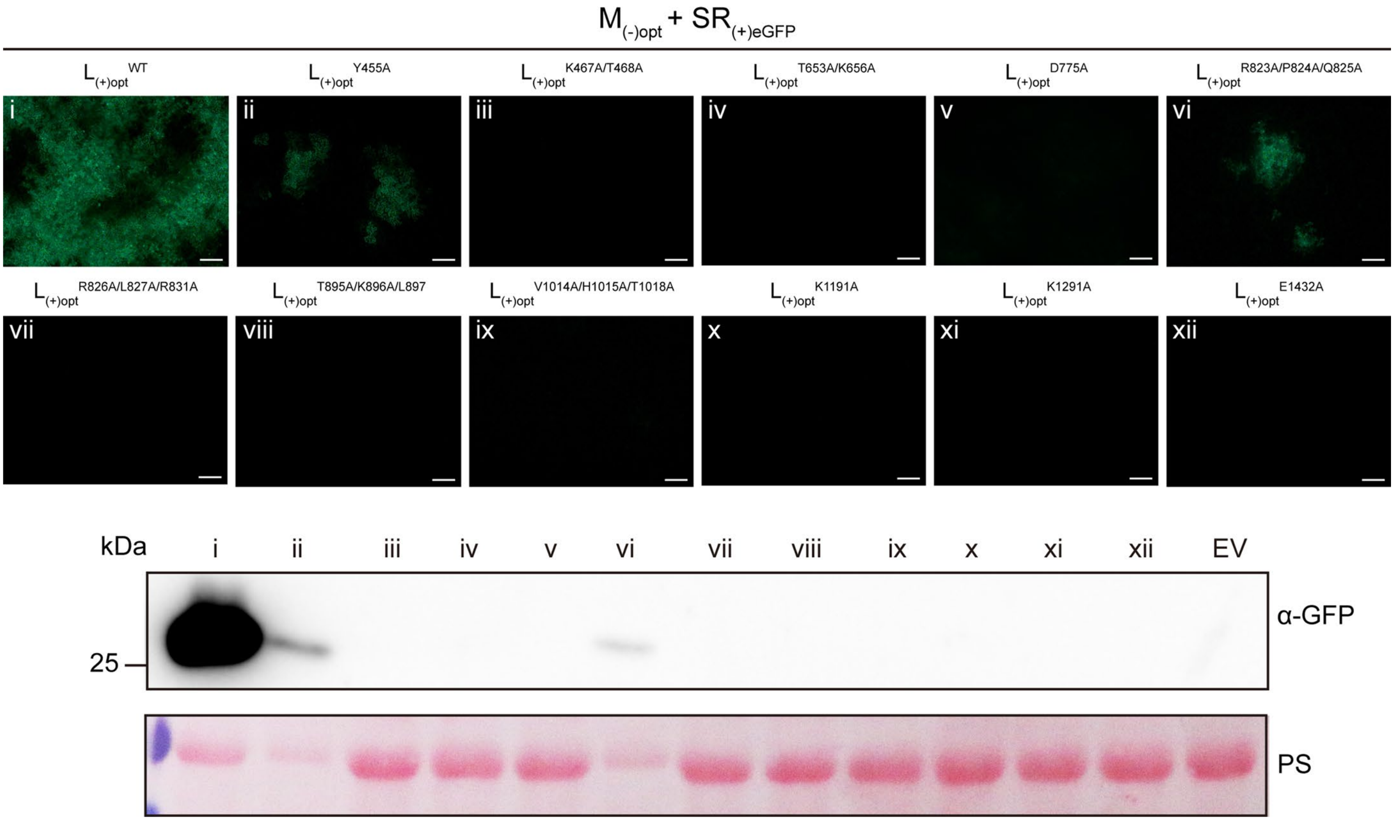

Extended Data Fig. 7 | Effect of key residues on the L protein that interact with 5′ 'hook' RNA on the rescue of TSWV. N. benthamiana leaves were inoculated with wild-type (WT) TSWV infectious clone [$L_{(+)opt}$+$M_{(-)opt}$+$SR_{(+)eGFP}$] and its mutants via agro-infiltration. Accumulation of eGFP fluorescence expressed from TSWV replicon in N. benthamiana leaves was detected with a fluorescence microscope at 60 h post inoculation (upper panel). Scale bars, 200 µm. Western blotting analysis of eGFP protein accumulation shown in lower panel using a GFP-specific antibody. The RuBisCO large subunit was stained with Ponceau S (PS) to indicate sample loading.

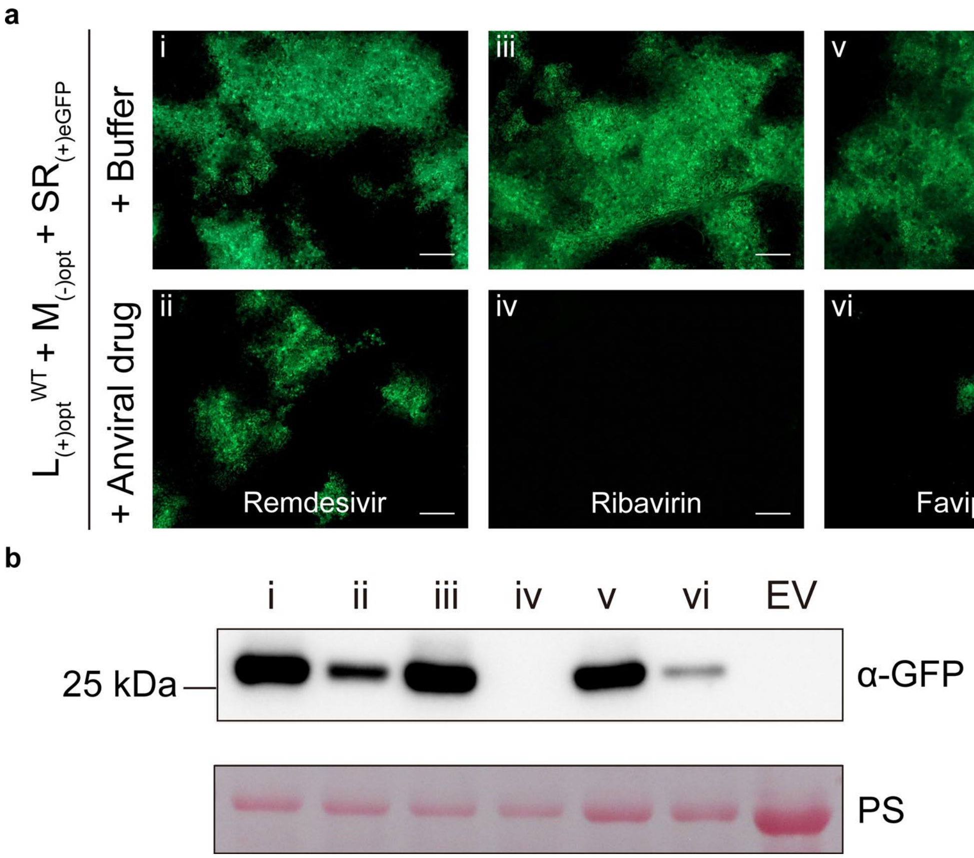

Extended Data Fig. 8 | Screening of antiviral drugs effective against TSWV using a micro-replicon system. a, Anti-TSWV activity of remdesivir, ribavirin and favipiravir were investigated using a micro-replicon system combined with a traditional half-leaf-inoculation method. N. benthamiana leaves were inoculated with wild-type (WT) TSWV infectious clone [$L_{(+)opt}$+$M_{(-)opt}$+$SR_{(+)eGFP}$] via agro-infiltration. The left side of the leaf was then subjected to treatment with the antiviral drug, while the right side was treated with a buffer solution. Accumulation of eGFP fluorescence expressed from TSWV replicon in N. benthamiana leaves was detected with a fluorescence microscope at 60 h post inoculation. Scale bars, 200 μm. **b**, Western blotting analysis of eGFP protein accumulation for various treatments shown in panel (a) using a GFP-specific antibody. The RuBisCO large subunit was stained with Ponceau S (PS) to indicate sample loading.

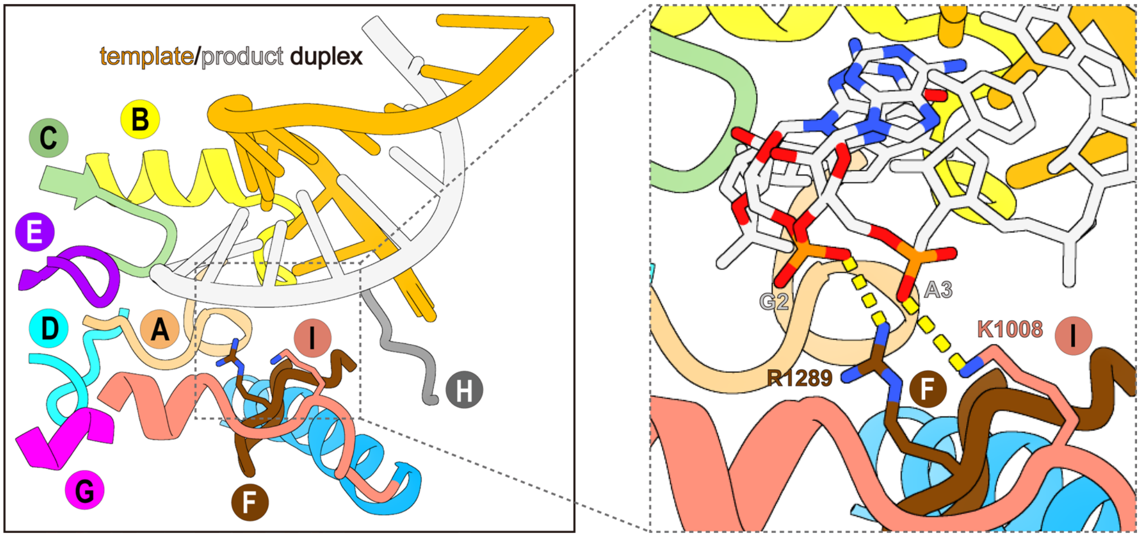

Extended Data Fig. 9 | Model for the elongation conformation of TSWV based on superposition with the HTNV polymerase (PDB: 8C4V) elongation complex structures. The template-product duplex RNA of HTNV was modeled into the active site of TSWV polymerase. The K1008 residue of TSWV L makes an ionic contact with the product strand phosphate group of A3. This would trap the tip of the Motif F finger sequence underneath of itself, fully structuring Motif F for NTP binding and activity. This is discussed further in the text.

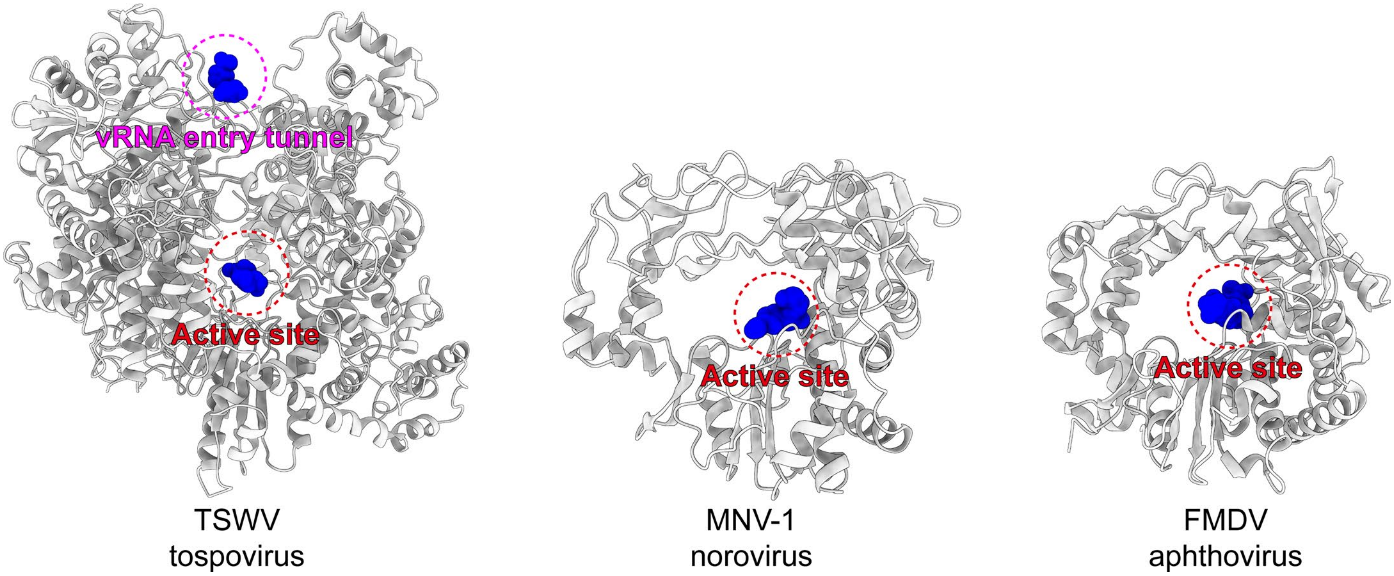

Extended Data Fig. 10 | Comparison of the binding site of ribavirin or its triphosphate on viral polymerases. Ribavirin and ribavirin triphosphate located in the vRNA entry channel and active site of TSWV polymerase are marked with magenta and red circle, respectively (left). Ribavirin located in the active site of MNV-1 (PDB ID: 3SFU, middle) polymerase and ribavirin triphosphate located in the active site of FMDV (PDB ID: 2E9R, right) polymerase are marked with red circle.

nature portfolio

Corresponding author(s): Xiangxi Wang

Last updated by author(s): Jan 11, 2025

Reporting Summary

Nature Portfolio wishes to improve the reproducibility of the work that we publish. This form provides structure for consistency and transparency in reporting. For further information on Nature Portfolio policies, see our Editorial Policies and the Editorial Policy Checklist.

Statistics

For all statistical analyses, confirm that the following items are present in the figure legend, table legend, main text, or Methods section.

n/a	Confirmed	
☐	☒	The exact sample size (*n*) for each experimental group/condition, given as a discrete number and unit of measurement
☐	☒	A statement on whether measurements were taken from distinct samples or whether the same sample was measured repeatedly
☐	☒	The statistical test(s) used AND whether they are one- or two-sided *Only common tests should be described solely by name; describe more complex techniques in the Methods section.*
☒	☐	A description of all covariates tested
☐	☒	A description of any assumptions or corrections, such as tests of normality and adjustment for multiple comparisons
☐	☒	A full description of the statistical parameters including central tendency (e.g. means) or other basic estimates (e.g. regression coefficient) AND variation (e.g. standard deviation) or associated estimates of uncertainty (e.g. confidence intervals)
☐	☒	For null hypothesis testing, the test statistic (e.g. *F*, *t*, *r*) with confidence intervals, effect sizes, degrees of freedom and *P* value noted *Give P values as exact values whenever suitable.*
☒	☐	For Bayesian analysis, information on the choice of priors and Markov chain Monte Carlo settings
☒	☐	For hierarchical and complex designs, identification of the appropriate level for tests and full reporting of outcomes
☒	☐	Estimates of effect sizes (e.g. Cohen's *d*, Pearson's *r*), indicating how they were calculated

Our web collection on statistics for biologists contains articles on many of the points above.

Software and code

Policy information about availability of computer code

Data collection	Micrographs were collected using SerialEM automated data collection software; Western and northern blots data were collected by Bio-Rad ChemiDocTM Touch Imaging System; Fluorescence and Images were captured with Image-Pro software (Olympus); Photographing of plant using Canon EOS 70D digital camera.
Data analysis	The raw micrographs data were processed by MotionCor2; The defocus value for each micrograph was determined using Gctf; The high quality particles were picked and extracted for two-dimensional alignment using RELION (v3.07); The quality of the local resolution was evaluated by ResMap; In addition, local refinement and DeepEMhancer were used for further improving the quality of CTD's map. The initial structure model was built using the AutoBuild program in Phenix and further corrected manually by real-space refinement in COOT (v1.1.11).

For manuscripts utilizing custom algorithms or software that are central to the research but not yet described in published literature, software must be made available to editors and reviewers. We strongly encourage code deposition in a community repository (e.g. GitHub). See the Nature Portfolio guidelines for submitting code & software for further information.

Data

Policy information about availability of data

All manuscripts must include a data availability statement. This statement should provide the following information, where applicable:

- Accession codes, unique identifiers, or web links for publicly available datasets
- A description of any restrictions on data availability
- For clinical datasets or third party data, please ensure that the statement adheres to our policy

The cryo-EM maps and atomic models have been deposited at the Electron Microscopy Data Bank and the Protein Data Bank with accession codes EMDB: 37256, and PDB: 8KIA (TSWV L apo state), EMDB: 37253, and PDB: 8KI7 (TSWV L-3'5'v RNA), EMDB: 37254, and PDB: 8KI8 (TSWV L-5'v RNA), EMDB: 37255, and PDB: 8KI9 (TSWV L containing CTD), EMDB: 37252, and PDB: 8KI6 (TSWV L-RBV bound), EMDB: 61241, and PDB: 9J8V (TSWV L-RBT bound). All data are available within this article and its supplementary files. All constructs are available upon request.

Research involving human participants, their data, or biological material

Policy information about studies with human participants or human data. See also policy information about sex, gender (identity/presentation), and sexual orientation and race, ethnicity and racism.

Reporting on sex and gender	This study did not generate these data.
Reporting on race, ethnicity, or other socially relevant groupings	This study did not generate these data.
Population characteristics	This study did not generate these data.
Recruitment	This study did not generate these data.
Ethics oversight	This study did not generate these data.

Note that full information on the approval of the study protocol must also be provided in the manuscript.

Field-specific reporting

Please select the one below that is the best fit for your research. If you are not sure, read the appropriate sections before making your selection.

☒ Life sciences ☐ Behavioural & social sciences ☐ Ecological, evolutionary & environmental sciences

For a reference copy of the document with all sections, see nature.com/documents/nr-reporting-summary-flat.pdf

Life sciences study design

All studies must disclose on these points even when the disclosure is negative.

Sample size	Three plants were used for each transient expression and virus inoculation assay. We did not add more sample sizes as the results were reproducible with the same trend. No statistical methods were used to predetermine sample size. Sample size was determined based on previous publications.
Data exclusions	No data were excluded from the analyses in this study.
Replication	Each experiment was repeated three times. Results were reproducible with the same trend.
Randomization	Allocation of test plants used in our study was random. There was no targeted selection of individual plants for specific treatments.
Blinding	Blinding was not used in our study. In plant, biology blinded/double-blinded studies are uncommon.

Reporting for specific materials, systems and methods

We require information from authors about some types of materials, experimental systems and methods used in many studies. Here, indicate whether each material, system or method listed is relevant to your study. If you are not sure if a list item applies to your research, read the appropriate section before selecting a response.

Materials & experimental systems

n/a	Involved in the study
☐	☒ Antibodies
☐	☒ Eukaryotic cell lines
☒	☐ Palaeontology and archaeology
☒	☐ Animals and other organisms
☒	☐ Clinical data
☒	☐ Dual use research of concern
☐	☒ Plants

Methods

n/a	Involved in the study
☒	☐ ChIP-seq
☒	☐ Flow cytometry
☒	☐ MRI-based neuroimaging

Antibodies

Antibodies used	Primary antibodies: anti-GFP (1:5,000, Sigma-Aldrich, Cat# SAB4301138), anti-TSWV L (1:500, Lab-made), anti-TSWV NP (1:10,000, Lab-made) Secondary antibodies: HRP-conjugated goat anti-rabbit (1:10,000, Sigma-Aldrich, Cat# A6154) and goat anti-mouse (1:10,000, Sigma-Aldrich, Cat# A4416)
Validation	In this study, antibody signals of TSWV L specific to the predicted molecular weight size were detected in plants expressing TSWV L or its mutant proteins and were not detected in plants not expressing TSWV L protein, indicating that the antibodies of TSWV L can be used; The GFP antibody signals were consistent with the antibody signals in the instructions provided by the manufacturer (https://www.sigmaaldrich.cn/CN/zh/product/sigma/sab4701015); Antibody signals of TSWV NP were consistent with literature data (Feng et al., 2020, PNAS).

Eukaryotic cell lines

Policy information about cell lines and Sex and Gender in Research

Cell line source(s)	SF9 insect cells (11496015, Invitrogen) and High Five cells (B85502, Invitrogen)
Authentication	We declare that none of the cell lines used were authenticated.
Mycoplasma contamination	We declare that the cell lines were not tested for mycoplasma contamination.
Commonly misidentified lines (See ICLAC register)	The study did not use any of the commonly misidentified cell lines.

Dual use research of concern

Policy information about dual use research of concern

Hazards

Could the accidental, deliberate or reckless misuse of agents or technologies generated in the work, or the application of information presented in the manuscript, pose a threat to:

No	Yes
☒	☐ Public health
☒	☐ National security
☒	☐ Crops and/or livestock
☒	☐ Ecosystems
☒	☐ Any other significant area

Experiments of concern

Does the work involve any of these experiments of concern:

No	Yes	
☒	☐	Demonstrate how to render a vaccine ineffective
☒	☐	Confer resistance to therapeutically useful antibiotics or antiviral agents
☒	☐	Enhance the virulence of a pathogen or render a nonpathogen virulent
☒	☐	Increase transmissibility of a pathogen
☒	☐	Alter the host range of a pathogen
☒	☐	Enable evasion of diagnostic/detection modalities
☒	☐	Enable the weaponization of a biological agent or toxin
☒	☐	Any other potentially harmful combination of experiments and agents

Plants

Seed stocks	Seeds of wild-type N. benthamiana plants were provided by Key Laboratory of Integrated Management of Crop Disease and Pests, Ministry of Education, Nanjing, China
Novel plant genotypes	No novel plant genotypes were produced in this study.
Authentication	No novel plant genotypes were produced in this study and we declare that the seeds of wild-type N. benthamiana plants used were not authenticated.